Controlled electron transfer by molecular wires embedded in ultrathin insulating membranes for driving redox catalysis

Heinz Frei

Molecular Biophysics and Integrated Bioimaging Division, Lawrence Berkeley National Laboratory, University of California, Berkeley, CA 94720

e-mail: HMFrei@lbl.gov

(*Photosynth. Res.* **159** (2023). DOI: 10.1007/s11120-023-01061-7)

Abstract

Organic bilayers or amorphous silica films of a few nanometer thickness featuring embedded molecular wires offer opportunities for chemically separating while at the same time electronically connecting photo- or electrocatalytic components. Such ultrathin membranes enable the integration of components for which direct coupling is not sufficiently efficient or stable. Photoelectrocatalytic systems for the generation or utilization of renewable energy are among the most prominent ones for which ultrathin separation layers open up new approaches for component integration for improving efficiency. Recent advances in the assembly and spectroscopic, microscopic and photoelectrochemical characterization have enabled the systematic optimization of the structure, energetics and density of embedded molecular wires for maximum charge transfer efficiency. The progress enables interfacial designs for the nanoscale integration of the incompatible oxidation and reduction catalysis environments of artificial photosystems and of microbial (or biomolecular)-abiotic systems for renewable energy.

1. Introduction

Ultrathin soft and hard matter layers enable the coupling of important photo- and electrocatalytic components that otherwise are difficult to integrate. The main reasons for the need of such layers include the separation of incompatible chemical environments because of the instability of certain components such as molecular light absorbers when exposed to photocatalytic intermediates or products, or because of efficiency-degrading back and side reactions upon coupling oxidation and reduction catalysis on the nanoscale. This holds for abiotic photoelectrocatalytic systems, in particular those for artificial photosynthesis, and for coupled biotic-abiotic catalysts of enzyme-based or microbial biohybrids. Moreover, some biological components like enzymes integrated with abiotic catalysts exhibit superior stability and charge transfer efficiency when absorbed on lipid bilayer films rather than directly interacting with the surface of an inorganic catalyst.

An essential property of ultrathin membranes for electro- and photocatalytic systems is efficient electron transfer from one side to the other, which requires tight control of the charge transport pathways and rates that are adequate for the intended use. Bazan pioneered intercalation of conjugated oligoelectrolyte molecules into lipid bilayers of a few nm thickness for imparting electron conductivity on insulating soft matter membranes (Garner et al. 2010; Yan et al. 2015). Exploration of a broad range of applications well beyond photo- and electrocatalysis has emerged from this approach in recent years, ranging from optical sensing, photovoltaics, electronics, to antimicrobial treatment and intercellular communication (Yan et al. 2015; Zhou et al. 2022). Using similar types of molecular wires, Frei and coworkers have developed methods for introducing charge conductivity into ultrathin (few nm thick) insulating inorganic oxide membranes, specifically amorphous silica layers. Combined with the excellent proton

permeability of ultrathin amorphous silica and its ability to block crossover of small molecules including oxygen, these robust nanomembranes enable the coupling of incompatible harsh catalytic reactions like those characteristic for artificial photosynthesis (Kim et al. 2016; Edri et al. 2018; Jo et al. 2022; Frei 2023). This approach opens up the development of nanoscale integrated artificial photosystems thereby minimizing efficiency-degrading processes endemic to macroscale photoelectrochemical systems. Ultrathin silica membranes offer similar advantages for the coupling of microbial catalysts with inorganic photo- or electrocatalysts on the nanoscale, opening up the development of nanobiohybrids that integrate microbial with inorganic catalysts for converting the energy of waste organics to drive inorganic electrocatalysis (Cornejo et al. 2018) or for powering microbial electrosynthesis by the charges generated with inorganic solar water splitters.

In this article, recent progress in the assembly, structural characterization and evaluation of the performance of charge conducting ultrathin organic and silica membranes based on the embedded molecular wire approach is discussed. Spectroscopic and microscopic methods for the structural characterization of (photo)electrochemical systems and the current understanding of the mechanism of charge transport via embedded molecular wires are presented. Particular emphasis is on how to improve the efficiency of abiotic or microbial/abiotic hybrid catalytic systems by optimizing wire energetics, geometry and density using electrochemical and time-resolved spectroscopic measurements.

2. Organic membrane-intercalated conjugated oligoelectrolytes

Lipid bilayers play a key role in living organisms as cell barriers and means of compartmentalizing biochemical functions. Inspired by Nature, bilayers were explored in the past two decades as electron conducting membranes by intercalating molecular wires in the form of conjugated oligoelectrolytes. After discussing the assembly, structural and functional characterization of wire-intercalated bilayer membranes, this section will focus on recent progress in utilizing these membranes for developing efficient biotic-abiotic interfaces.

2.1 Synthesis and characterization

The initial work on intercalating oligoelectrolytes into lipid bilayers (Garner et al. 2010) utilized phospholipids with alkane chains of 14 carbons (1,2-dimyristoyl-*sn*-glycero-3-phosphocholine, DMPC) or 16 carbons (1,2–dipalmitoyl-sn-glycero-3-phosphocholine (DPPC), shown in Figure 1. For molecular wires, π-delocalized phenylenevinylene chains were chosen as linear rigid backbones terminated on both ends with pendant moieties featuring ammonium groups. Specifically, terminally charged DSBN+ (1,4-bis(4'-(N,N-bis(6"-(N,N,N-trimethylammonium)hexyl)amino)-styryl)benzene tetraiodide) or DSSN+ (4,4'-bis(4'-(N,N-bis(6"-(N,N,N-trimethylammonium (hexyl)amino)-styryl)stilbene tetraiodide) molecules were used, with dimensions that closely match the ~4 nm thickness of the lipid bilayer (Figure 1) (Gaylord et al. 2001; Woo et al. 2005; Garner et al. 2010; Yan et al. 2015).

Of critical importance for the assembly process and efficient electron transfer through the membrane are the spatial order and, in particular, the orientation of the intercalated conducting molecules. Detailed characterization was provided by a combination of polarized UV-vis absorption and photoluminescence spectroscopy, confocal microscopy, and cryogenic transmission electron microscopy. As shown in the confocal fluorescence microscopic image of

a stationary DMPC vesicle with intercalated DSBN+ molecules of Figure 2a, excitation of DSBN+ with polarized 488 nm light results in attenuated emission for regions in which the long axis of the molecules is oriented perpendicular to the plane of the excitation beam (Figure 2b) while there is strong emission of DSBN+ oriented parallel to the plane of excitation (Figure 2c). These observations demonstrate the ordered intercalation of the DSBN+ wire molecules into the lipid bilayer with the long axis of the wire molecules orientated perpendicular with respect to the plane of the membrane. This orientation is mainly due to charge compensation between the zwitterions in DMPC and the terminal quaternary ammonium ions of DSSN+ combined with the hydrophobic interactions between neutral parts of DSSN+ and the alkyl chains of DMPC (Garner et al. 2010; Yan et al. 2015).

The electron transport properties of the membrane-embedded molecular wires were evaluated by cyclic voltammetry (CV) using a glassy carbon electrode coated by the lipid bilayer exposed to aqueous ferricyanide solution. The strong ferricyanide/ferrocyanide CV wave of DSSN+ containing DPPC bilayer membranes (2 percent loading) shown in Figure 3a (red trace) compared to the negligible signal of the wire-free insulating bilayer (green trace) demonstrates the electron conductivity imparted by the embedded oligo(phenylenevinylene) molecules. The tunneling current through the membrane reaches 75 percent of the electron flux of the bare glassy carbon electrode (black CV trace), supporting the conclusion that the wire molecules span the bilayer side-to-side as expected from the normal orientation to the plane of the membrane. Comparison of the CV result of this intercalated bilayer membrane with that of the slightly shorter DSBN+ embedded in DPPC bilayer (Figure 3b, orange trace) shows a ~50 percent smaller current for the latter (Garner et al. 2010). The observed sensitivity of the wire length on the electron transport efficiency indicates that the oligo(phenylenevinylene) backbone with 4 aryl

units more completely spans the membrane compared to the shorter wire with 3 aryl units. The effect of the length of the phospholipid molecules on the electron transport (DPPC versus DMPC), while significant according to the CV results shown in Figure 3, is much smaller by comparison.

For oligo(phenylenevinylene) molecular wires with 4 or more aryl units, the π-delocalization is sufficiently large for the emission spectrum to extend from the UV into the visible spectral region. This offers opportunities for exploiting Foerster resonance energy transfer (FRET) of excited wires to visible light absorbing dyes for boosting photovoltaic efficiency (Lee et al. 2013). A case study of this effect is a photovoltaic system in which a film of Nile red, a strong visible dye, tethered in an alkanethiol self-assembled monolayer (11-mercaptoundecanoic acid) on a gold electrode is covered by a precisely interfaced DMPC/DSSN+ lipid bilayer, as depicted in Figure 4a. As shown in Figure 4b, the optical absorption of Nile red overlaps well with the emission of DSSN+ in the lipid environment resulting in extensive FRET that enhances the efficiency of the photovoltaic assembly. This is shown in Figure 4c by the linear increase of Nile red emission with increasing dye concentration when exciting DSSN+ at 400 nm, a wavelength at which no light is directly absorbed by the dye. The rise time of the Nile red emission was ultrafast (200 ps), characteristic for FRET mechanism. For 2.5 percent loading of dye in alkane thiol bilayer, a high FRET efficiency of 93 percent was determined by steady-state and ultrafast photoluminescence and absorption spectroscopy. Using ascorbic acid as electrolyte, the photocurrent density was boosted by 36 percent for the DMPC/DSSN+/Nile red/gold assembly compared to the photocurrent superposition of bare Nile red/gold and DMPC/DSSN+/gold layers (Figure 4d) (Lee et al. 2013).

2.2 Developing efficient biotic-abiotic interfaces using organic membrane-intercalated oligoelectrolytes

Ultrathin organic membranes based on conjugated oligoelectrolytes have opened up exciting approaches for designing interfaces for integrating biological with abiotic function. For example, Nature's Photosystem I protein complex (PSI) interfaced with the flat surface of a lipid bilayer/DSSN+ membrane, which is tied to a gold electrode surface by 1,2-dipalmitoyl-*sn*-glycerol-phosphothioethanol as shown in Figure 5a (Saboe et al. 2014) exhibits a two orders of magnitude increase of the photocurrent compared to PSI crystals directly deposited on the electrode. The latter is coated with a self-assembled monolayer (SAM) of a small molecule (e.g. nitrilotriacetic acid (Krassen et al. 2009) or functionalized hexanethiol molecules (Manocchi et al. 2013). CV sweeps shown in Figure 5b confirm that the redox waves of an appropriate couple like ferricyanide/ferrocyanide are only observed for the bilayer membrane with embedded DSSN+ wires (blue dashed trace), but not for bilayer without DSSN+ (red dashed trace). The hydrophobic lipid bilayer mimics the thylakoid membrane environment which the protein complex resides in in the natural system, with the flat surface providing a perfect interface for high density 2-dimensional crystalline PSI arrays (weight lipid-to-protein ratio ~1) (Saboe et al. 2014). With the PSI layer exposed to aqueous solution of methyl viologen (MV^{2+}) electron acceptor, visible light excitation of the protein resulted in electron transfer from its reducing side of PSI to MV^{2+}. Concurrently, the oxidized PSI is reduced by electrons delivered from the Au surface through the bilayer membrane via DSSN+ wires. The solid trace of the photocurrent on/off experiment of Figure 5c shows a high value of 17 μA cm^{-2}. The photocurrent of this PSI/DSSN+-bilayer assembly on Au electrode exceeds 4-fold the photocurrent in the absence of embedded molecular wire (Figure 5c, dashed trace). A small photocurrent of 3 μA cm^{-2} observed

for the membrane with embedded wires but omitting PSI, shown by the dashed-dot trace in Figure 5c, originates from direct photoexcitation of DSSN+ wires.

The fragility of lipid bilayers has motivated the exploration of block copolymer bilayers as replacement material for insulating ultrathin membranes. PSI photosynthetic protein was stabilized in a block copolymer environment of composition poly(butadiene)$_{12}$-poly(ethylene oxide)$_8$ (PB_{12}-PEO_8), as sketched in Figure 6a (inset on the right). This assembly was deposited on a PB_{12}-PEO_8 bilayer membrane with embedded DSSN+ wire molecules (Figure 6a) (Saboe et al. 2016). The conducting ~4 nm thick membrane is substantially more stable than lipid bilayer membranes by virtue of stronger hydrophobic interaction of PB_{12}-PEO_8 polymers and their ability to cross-link. The CV sweeps of Figure 6b show that ferricyanide/ferrocyanide redox waves are only observed for the block copolymer bilayer membrane with embedded DSSN+ wires (solid green trace) but not for the bare PB-PEO membrane (dotted blue trace). As indicated by Figure 6c, visible light excitation of the PSI-block copolymer/PB-PEO/DSSN+ assembly on gold electrode results in 35 $\mu A\ cm^{-2}$ photocurrent density (green trace), which is twice as large as for the corresponding lipid bilayer construct. Importantly, sustained photocurrent was observed for a period of a month, by far exceeding the stability of lipid bilayer-based constructs.

Of particular interest is embedding of molecular wires into microbial lipid bilayer membranes for enhancing the efficiency of bioelectrochemical systems such as microbial fuel cells and microbial electrosynthesis cells. In microbial fuel cells, an organism converts organic compounds such as carbohydrates or organic waste products to CO_2, with the electrons collected at the anode generating electricity upon transfer to the cathode for O_2 (or inorganic ion) reduction (Yan et al. 2015). Conversely, microbial electrosynthesis cells use CO_2-fixing microbes on the cathode for the reduction to high energy carbon compounds or valuable

industrial organics, with the electrons generated under applied potential at the anode, most often by H_2O oxidation (Nevin et al. 2010; Rabaey and Rozendal 2010). Imaging by confocal microscopy confirms ready intercalation of DSSN+ and other conjugated oligoeletrolytes into membranes of yeast, *Shewanella oneidensis*, *E. coli* or mammalian cells (Du et al. 2013; Hou et al. 2013; Thomas et al. 2013; Yan et al. 2015). Electrochemical measurements demonstrate substantial efficiency enhancement of fuel cells or electrosynthetic devices upon molecular wire intercalation (Kirchhofer et al. 2014). However, the mechanism of electron transfer enabled by the wire molecules is more complex for these microbial systems than for organic bilayer membranes and may include multiple operating pathways. In contrast to abiotic systems, mechanisms for organisms tend to be less definitive at the current stage.

For microbial electrosynthesis, *S. oneidensis* exhibits two established mechanisms for electron transfer to an anode surface. One pathway for electrons arriving from the inside of the cell at membrane-bound cytochromes (termed MtrC and OmcA), located on the outer cell membrane, consists of direct transfer from the cytochrome to the electrode surface or via biosynthesized nanowires that span the gap between the outer cell membrane and the electrode surface (Baron et al. 2009; El-Naggar et al. 2010). The second pathway consists of redox shuttle molecules, principally flavin-based species, that transfer electrons by diffusion from MtrC or OmcA to the electrode surface (Lovley 2008; Marsili et al. 2008; Coursolle et al. 2010). A variant of flavin enhanced electron transfer is the formation of a complex with the outer membrane cytochromes that results in 3-5 orders of magnitude increase of electron transfer to the external electrode surface without necessitating redox-shuttling between cytochromes and electrode (Okamoto et al. 2013).

Based on the distinctly different, characteristic redox potentials of the direct electron transfer and electron shuttle-mediated transfer (Baron et al. 2009; Roy et al. 2014), the enhancement effect of DSSN+ was attributed to the direct electron transfer pathway, which is independent of the shuttle-mediated mechanism (Kirchhofer 2014). Figure 7 shows the result of chronoamperometric measurements of *S. oneidensis* colonies absorbed on a graphite anode. For calibration, the red and black traces displayed on the left hand side of the figure indicate the current density behavior of two identical microbe-covered anodes over a period of 23 h. Maximum current is observed 4 h after poising the anode at +0.2 V vs. Ag/AgCl that initiates bacterial conversion of lactate (time point I in Figure 7), followed by leveling off around 20 h (stop at 20.4 h, marked time point II). After replacement of the bacterial colonies on the anodes by fresh ones (III), 5 μM DSSN+ is added to one sample (labeled Type 2, red trace) but not to the control sample (labeled Type 1, black trace). Upon application of the +0.2 V bias in the presence of lactate, a large increase of the bacterial current is observed for the DSSN+ loaded sample (red trace on the right of time point 24.1 h (IV) to 44.5 h (VI), with the total charge exceeding the charge in the absence of DSSN+ by a factor of 2.2. At the same time, the microbial colonization mass increases by a factor of 3.1, which corresponds to an increase of the current efficiency from 51 to 84 percent upon introduction of DSSN+ (Kirchhofer et al. 2014). As the comparison of this sample with the control shows (time point IV), the boosting effect of the DSSN+ occurs within less than 160 s. This is far too fast for any growth of the microbial colony to play a role, which demonstrates that the molecular wires enhance the rate of direct, one-electron transfer between the native outer membrane cytochromes and the electrode surface. It shows that the amphiphilic membrane-bound MtrC and OmcA cytochromes are accessible for close contact with the amphiphilic DSSN+ molecules. In this way, the aromatic core of DSSN+

increases the electronic surface area of the cytochromes and thereby explains the enhancement of the direct electron transfer rate.

3. Amorphous silica membrane-embedded molecular wires

Embedding of molecular wires into ultrathin insulating inorganic oxide instead of soft matter layers might offer opportunities for robust electron and proton conducting membranes that are needed for systems involving harsh reaction conditions such as those of artificial photosynthesis. The section focuses on assembly methods and infrared spectroscopic techniques for the structural characterization of the composite membranes. This is followed by photoelectrochemical measurements for identifying optimal energetics and density of embedded wire molecules, and ultrafast optical spectroscopy for determining the charge transfer mechanism. Examples which demonstrate how these silica layers with embedded wires enable the development of complete nanoscale artificial photosynthetic units with built-in membrane separation, and the coupling of microbial-abiotic systems on the nanoscale will be presented.

3.1 Assembly and structural characterization

At the heart of the challenge for making complete photosystems that use the energy of the sun for converting H_2O and CO_2 to energy dense fuels is the electronic and protonic coupling of H_2O oxidation and CO_2 reduction. These reactions take place in catalysis environments that are incompatible. If not separated by a membrane that blocks crossover of small molecules and intermediates, back and side reactions will invariably degrade photosynthetic efficiency. This holds in particular for integration on the nanoscale, which is advantageous because coupling on

the shortest possible length scale minimizes efficiency losses inherent to the macroscale, in particular the transport resistance of ions and the limited control of the movement of charges, protons, and molecular species as already noted for organic membranes. We have found that ultrathin amorphous silica layers of few nm thickness possess the desired properties for encapsulating oligo(phenylenevinylene) wire molecules while providing adequate proton conductivity and chemical separation of small molecules including O_2, as discussed in the following (Kim et al. 2016; Jo et al. 2022; Frei 2023).

Our approach consists of inserting an amorphous silica membrane of a few nm thickness with embedded molecular wires between the visible light absorber and a solid metal oxide catalyst for water oxidation (Co_3O_4), as sketched in Figure 8a. In this way, the sites of H_2O oxidation and evolving O_2 are blocked off from the sites of light absorption (all-inorganic ZrOCo heterobinuclear metal-to-metal charge-transfer units) and the space of CO_2 reduction and evolving hydrocarbon products. With the goal of coupling light driven CO_2 reduction and H_2O oxidation in nanosized photosynthetic units with morphology suitable for forming macroscale assemblies that retain the membrane separation property, we chose nanotube morphology. In parallel, planar membrane analogues with the same chemical composition as the nanotubes were deposited on Pt electrodes for quantitative (photo)electrochemical characterization. Corresponding spherical nanoparticles enabled us to conduct ultrafast optical absorption spectroscopy for unraveling the charge transfer mechanism.

Essential structural requirements of embedded molecular wires in amorphous silica are the integrity of the organic molecule upon encapsulation in the SiO_2 and that they span the layer side-to-side. To accomplish the latter, oligo(phenylenevinylene) molecules with 3 aryl units (distyryl benzene, abbrev. PV3) were covalently linked to tripodal aryl anchors on the surface of

the Co_3O_4 catalyst. As illustrated in Figure 8b, 4-(trimethoxysilyl)aniline (TMSA) anchor reacts with surface OH groups of Co_3O_4 resulting in vertical orientation of the aniline ring axis relative to the oxide surface (Katsoukis and Frei 2018; Katsoukis et al. 2019). Hence, subsequent attachment of the PV3 molecule, featuring a carboxyl group in *p* position, to the anchor by an amide bond results in vertical orientation of the molecular wire axis.

Two surface sensitive infrared spectroscopic techniques, polarized FT-infrared reflection absorption spectroscopy (FT-IRRAS) and non-polarized grazing angle attenuated total reflection FT-infrared spectroscopy (GATR FT-IR) are well suited for verifying the structural integrity and for determining the orientation of the surface attached wire molecules (Katsoukis et al. 2019). These techniques require planar samples, which were obtained by depositing Co_3O_4 layers on planar Pt surface by atomic layer deposition (ALD) followed by the attachment of wires and casting into amorphous silica by ALD (Figure 8b). The surface sensitivity of the FT-IRRAS technique stems from the fact that the electric field of the infrared probe beam perpendicular (p) to the sample surface is amplified by up to a factor of four upon reflection at the Pt surface, while the horizontal electric field component (s) parallel to the Pt surface is cancelled (metal surface selection rule). Therefore, vibrational modes perpendicular to the surface absorb infrared light while vibrational components parallel to the surface do not, as shown in Figure 9a (Chabal 1988; Hollins 2006). By contrast, the evanescent wave of non-polarized GATR FT-IR spectroscopy probes both perpendicular and horizontal vibrational modes of the sample surface if held in μ distance from the ATR element (Figure 9a). Therefore, comparison of FT-IRRAS and GATR FT-IR spectra of the same sample allows us to determine the orientation of the embedded wire molecules.

Monitoring of the attachment of the PV3 wire molecules to TMSA anchored on Co_3O_4 by FT-IRRAS affords quantitative measurement of linkage formation as presented in the spectra of Figure 9b. Spectral trace (1) shows the attached TMSA anchor before, trace (2) after amide bond formation to PV3. Not only does the TMSA spectrum (1) confirm the vertical orientation of the tripodal TMSA anchor (Katsoukis et al. 2019), but trace (2) shows 90 percent loss of the intensity of the TMSA NH_2 bending mode at 1621 cm^{-1} under growth of the amide stretch (amide I mode) at 1666 cm^{-1}, allowing for accurate measurement of the fraction of anchors linked to a wire molecule (the remaining 10% are presumably not accessible by PV3 for amide bond formation). The orientation of the wire is determined by the comparison of p-polarized FT-IRRAS and non-polarized GATR FT-IR spectra of one and the same sample shown in Figure 9b trace (3) and trace (4), respectively. For facilitating the comparison, the TMSA infrared bands are subtracted from both spectra, i.e. traces (3) and (4) visualize exclusively the infrared spectra of PV3 modes of the surface attached wires. The most pronounced difference of the polarized and non-polarized infrared spectra is the out-of-plane CC-H bend mode at 963 cm^{-1} (blue shaded section of spectrum). This mode is intense in the GATR infrared spectrum, but completely absent in the IRRAS trace. Its absence in the IRRAS spectrum means that the mode oscillates parallel to the Pt (and Co_3O_4) surface. Because the oscillating direction is perpendicular to the aryl-vinyl backbone, the PV3 axis is oriented perpendicular to the Co_3O_4 surface. An estimate of the uncertainty of the wire orientation of 90^o relative to the surface gives $\pm 12^o$. Polarization dependent intensities of several other PV3 modes in the 2000-800 cm^{-1} region further support the vertical orientation of the wires (Katsoukis et al. 2019).

FT-IRRAS measurements are similarly useful for monitoring the casting of the molecular wires into silica and verifying the structural integrity and orientation in the membrane. The

observations provide a precise guide for optimizing the ALD protocol in order to minimize damage to the organic (Katsoukis et al. 2019). Figure 9c, black trace (1), shows the spectrum of the PV3 anchored on Co_3O_4 before deposition of SiO_2 by plasma-enhanced ALD (same sample as shown in Figure 9b trace (3) before subtracting TMSA bands). Deposition of 3 nm SiO_2 (20 ALD cycles) is readily monitored by the longitudinal optical asymmetric O-Si-O stretch mode at 1236 cm^{-1} characteristic of ultrathin amorphous silica layers (Figure 9c, red trace (2)) (Burton et al. 2009). The bands of PV3 and linked TMSA anchor exhibit the same relative intensities as before SiO_2 deposition, and no new absorptions are observed. This indicates that the structural integrity of wires and anchors are preserved, and the vertical orientation of the wire axis is not altered by the silica encasement. In addition to being imposed by the tripodal aryl-$Si(OCo)_3$ anchor, the vertical orientation is forced by the ALD process itself because silica grows on the metal oxide surface in the free spaces between the anchored organic molecules with a tendency to straighten them up (Son et al. 2012).

Because the length of the PV3 wire is commensurate with the 3 nm thickness of the ALD silica layer, the wires completely span the membrane. This is supported by Figure 9c, blue trace (3), recorded after deposition of additional 3 nm of SiO_2. An identical growth of the 1236 cm^{-1} SiO_2 band is observed, as expected, with no change of the wire spectrum. These infrared measurements afford a precise, detailed account of the structural integrity and orientation upon embedding of the attached molecular wires in the amorphous silica membrane. While most vibrational bands of the wire molecules do not exhibit a spectral signature of interaction with the SiO_2 environment, monitoring by FT-Raman spectroscopy revealed a small but significant blue shift of 9 cm^{-1} of the backbone aryl stretch at 1600 cm^{-1} upon SiO_2 casting that manifests weak interaction with the surrounding silica membrane (Katsoukis and Frei 2018).

3.2 Optimization of the electron transfer efficiency

Evaluation by short circuit photocurrent measurements of charge transfer from visible light absorbers across the silica membrane via molecular wires provided a sensitive method for quantifying and optimizing the efficiency. The planar $Pt/Co_3O_4/PV3/SiO_2$ sample whose infrared spectra is shown in Figure 9c is used as working electrode of a 3-electrode electrochemical cell (Figure 10a). The familiar $[Ru(bpy)_2(dcbpy)]^{2+}$ visible light photosensitizer, which has one bipyridyl ligand functionalized by carboxyl groups (dcbpy), was covalently anchored on the silica membrane surface using again the amide linkage to a tripodal aniline anchor (heterobinuclear light absorbers shown in Figure 8a are suitable for high surface area nanostructured morphologies such as nanotubes but need to be replaced by more strongly absorbing dyes to afford sufficient photocurrents in the case of planar samples). Visible light excitation in the presence of $S_2O_8^{2-}$ sacrificial electron acceptor generates $[Ru(bpy)_2(dcbpy)]^{3+}$ upon electron transfer to persulfate, resulting in cathodic photocurrent upon hole transfer through the embedded wire molecules to the Pt/Co_3O_4 layer (Figure 10b, red trace (1)) (Zhang et al. 2021). For a sample with identical composition but without embedded PV3 wires, no Faradaic photocurrent was measured as shown by the black trace (2) of Figure 10b. Here, only capacitive cathodic photocurrent spikes are observed, which are caused by the accumulation of unreduced $[Ru(bpy)_2(dcbpy)]^{3+}$ species (Zhang et al. 2021). The ultrathin silica membrane is free of pinholes as verified by CV measurements using standard redox couples (Figure 10d).

An important parameter for optimizing the charge transfer efficiency across the membrane is the density of the embedded wires. Optimization was enabled by the precise determination of the wire and light absorber loading by FT-IRRAS measurements of samples

used for photocurrent measurements. By measuring the intensity of the π-π* band of TMSA anchors (ε(246 nm) = 13,400 L mol cm^{-1}) by UV transmission spectroscopy of Co_3O_4/PV3/SiO_2/ $Ru(bpy)_2(dcbpy)$ samples deposited on a quartz slide and comparing it with the TMSA FT-IRRAS bands observed for an identical sample prepared on a Pt electrode, the density of the anchor could be accurately determined. The subsequent absorbance decrease of the TMSA NH_2 mode at 1621 cm^{-1} upon PV3 ($Ru(bpy)_2(dcbpy)$) attachment by amide bond formation gave the density of the wires (light absorbers) for each sample. Figure 10c shows that the photocurrent density increases linearly with increasing loading from 0.8 to 4 nm^{-2}, in agreement with the stronger electronic coupling and lower reorganization energy that result from a shortening of the average spatial separation of anchored light absorber and the terminal aryl ring of the embedded wire molecule (Marcus and Sutin 1985). Because the integrity of the silica separation membrane for blocking O_2 and other small molecules would degrade at higher embedded wire densities, the optimum wire density was determined to be 4–5 nm^{-2}. A much less pronounced sensitivity of the photocurrent was found when varying the light absorber density, which was explained by the balancing out of competing interfacial charge transfer processes (Zhang et al. 2021).

An equally influential parameter for maximizing the photocurrent density of the silica membrane is the energy level alignment of the embedded wires with light absorber and catalyst. As shown in the energy diagram of Figure 11a, efficient hole hopping across the membrane demands that the HOMO (highest occupied molecular orbital) of the embedded wire molecule is situated at more negative potential than the HOMO of the $[Ru(bpy)_2(dcbpy)]^{2+}$ complex on one side, and more positive relative to the potential of the Co_3O_4 catalyst on the other. To determine the optimum energy level alignment, the HOMO potential of PV3 was varied by introducing electron withdrawing groups (terminal C_6F_5 ring) or electron donating substituents (methoxy

(OMe)) in para (*p*) position of the terminal aryl moiety of the distyryl benzene backbone. Photocurrent measurements of silica membranes using these two wire modifications were compared with that of *p*-SO_3Et (Et = CH_2CH_3) terminated PV3 wire. All three wire modifications were attached to the tripodal silyl anchor by triazole linkage (click reaction between ethynyl terminated PV3 and azido functionalized tripodal silylbenzyl anchor). The *p*-SO_3Et derivatized PV3 with triazole linkage afforded comparison with the amide linked *p*-SO_3^- wire for probing the influence of the linker. The modified wire molecules using click attachment together with the corresponding FT-IRRAS data are presented in Figure 11c. The selection of the substituents was based on predictions of HOMO potentials by DFT calculations, which included the energetic effect of the amide versus triazole linkage. The HOMO potentials for all wires and alignment with light absorber and catalyst potentials are presented in Figure 11a (Zhang et al. 2021).

As the results of Figure 11b show, there is a strong HOMO potential dependence of the photocurrent. In addition to allowing identification of the optimal molecular wire, the data reveal key mechanistic insights on charge transfer across the membrane. Specifically, comparison of the photocurrent density of the triazole-linked wires (blue-labeled F_6, SO_3Et, OMe entries in Figure 11a and 11b) is most readily accessible to interpretation by electron transfer theory (Marcus and Sutin 1985) because of identical distyryl backbone, linker, and anchor attachment of these wires to the Co oxide surface. As a result, the reorganization energy and electronic coupling differences among them are very likely small compared to the free energy differences of hole transfer from the $[Ru(bpy)_2(dcbpy)]^{3+}$ to the wire HOMO (Step 1 in Figure 11a). The observed increase of the photocurrent density by a factor of 3 from the fluoro derivatized wire to the sulfonate ester wire is in agreement with the 70 mV stronger driving force of charge transfer Step

1. Furthermore, the absence of any photocurrent for the methoxy derivative reflects the fact that hole transfer from the wire HOMO to Co_3O_4 (Step 2 in Figure 11a) is endoergic by about 0.5 V. Comparison of the amide-linked SO_3^- functionalized wire with the triazole linked sulfonate wire shows 10 times larger photocurrent density for the latter (Figure 11c), in agreement with the 320 mV larger driving force of Step 1 for the triazole linked wire. Hence, the latter is the most efficient wire for hole transfer across the membrane (Zhang et al. 2021). Nevertheless, the observed photocurrent density of 33 nA cm^{-2} is far below what is needed for the charge flux through the membrane to keep up with the photon flux at maximum solar intensity. By replacing the sacrificial persulfate electron acceptor in solution, which cannot keep up with the photoactivation rate of the light absorber because of slow diffusion, with a more efficient solid oxide electron acceptor, here the conduction band of a TiO_2 nanolayer, photocurrents as high as 6.4 μA cm^{-2} are reached (Figure 10e). This result pertains to the comparatively inefficient amide-linked wire and as yet un-optimized wire density. Therefore, if replaced by the most efficient click-attached wire at optimal density of 5 nm^{-2}, a photocurrent of 0.1 mA cm^{-2} can be achieved. This current density for planar geometry translates to 10 mA cm^{-2} for an artificial photosystem with nanostructured architecture featuring 100-fold higher surface area such as the core-shell nanotube array presented below (10 mA cm^{-2} is adequate for keeping up with the photon flux at maximum solar intensity (Sun et al. 2017)).

While photocurrent measurements are best suited for quantitatively assessing and maximizing the charge flux across the membrane, ultrafast optical spectroscopy is required for elucidating the charge transfer mechanism. To facilitate analysis of ultrafast optical absorption data, a chromophore with established spectroscopic signature on the femto and picosecond timescale, such as porphyrin, is required. The spectral sensitivity of the measurement was

optimized by exploiting the high surface area of spherical Co_3O_4/PV3/SiO_2 core-shell nanoparticles. A free-base porphyrin with positively charged ligands was selected as light absorber to take advantage of its strong visible light absorption, matched redox potential for hole transfer to embedded PV3 wire molecules, and electrostatic attraction to the negatively polarized SiO_2 shell for strong surface adsorption (Edri et al. 2017). Upon excitation of the porphyrin at 430 nm with a 150 fs laser pulse, hole transfer to the embedded wire molecule was observed by PV3 radical cation absorption ($PV3^+$) at 1130 nm and concurrent rise of reduced porphyrin (H_2P^{red}) at 695 nm within hundreds of femtoseconds. The corresponding spectra are shown in Figure 12a and 12b, respectively. These observations confirm that the wire is transiently occupied by a hole charge. The decay of the bands on the tens of picosecond timescale is due to hole transfer to Co_3O_4, which competes with charge recombination of $PV3^+$ and H_2P^{red} (Figure 12d). The arrival of the hole charge on Co_3O_4 is monitored by the bleach with a maximum at 485 nm (Figure 12c, dark red trace, with the growth kinetics of the bleach shown in the inset of Figure 12d). A hole transfer time from the embedded wire to Co_3O_4 of 255 ps is derived from kinetic analysis (Edri et al. 2017). The ultrafast charge transport across the silica membrane revealed by these measurements means that it is likely to prevail over possible competing processes that otherwise would degrade the efficiency.

Maintaining charge balance during electron or hole transfer is an essential requirement for a functional membrane. Proton flow through the membrane most often plays this critical role and is particularly relevant for artificial photosystems that convert CO_2 and H_2O to fuel molecules; protons transmitted through the membrane combine with CO_2 and electrons at the catalytic reduction sites to form hydrocarbon product. Electrochemical impedance spectroscopy and CV measurements revealed that ultrathin amorphous silica layers sustain more than adequate

H^+ flux for keeping up with photocatalytic rates at maximum solar intensity. Equally importantly, they completely block crossover of small molecules including O_2 (Jo et al. 2020).

By meeting the requirements for a charge and proton conducting ultrathin separation membrane for artificial photosynthesis, silica nanolayers with embedded molecular wires enable the development of nanoscale units for the conversion of CO_2 and H_2O to fuel molecules. We selected Co_3O_4/PV3/SiO_2 core-shell nanotube geometry using the space on the inside for oxidation of H_2O vapor to O_2 at the Co oxide catalyst surface and the outside of the SiO_2 shell for light absorption and CO_2 reduction, as sketched in Figure 13a. In this way, the spaces of the incompatible catalysis environments are separated. A transmission electron microscopic (TEM) image of the wall of such a nanotube is shown in Figure 13b. By fabricating square inch sized nanotube arrays by atomic layer deposition techniques combined with the molecular wire embedding methods discussed above and sacrificial Si nanorod arrays as sacrificial template, macroscale nanotube arrays functionalized in the same manner as described for the planar samples were prepared. A scanning electron microscopic (SEM) image of a small section of such an array is shown in Figure 13c. With a top and bottom cover in place, the nanotube array geometry afford separation of the oxidation and reduction environment on all length scales from the nano to the macroscale (Kim et al. 2016; Edri et al. 2018; Jo et al. 2022).

Silica nanomembranes whose embedded molecular wires are optimized for the transfer of hole charges are essential for separating O_2 evolution catalysis from light absorption and CO_2 reduction catalysis of artificial photosynthesis systems. Wires suitable for efficient electron transfer are needed as well, e.g. for optimizing the overall conversion efficiency for CO_2 photoreduction by H_2O by replacing the single light absorber by a two-photon Z-scheme light absorber system. The hierarchical nature of the assembly method of core-shell nanotubes is

suitable for coupling of two light absorbers with complementary optical properties and matched redox potentials in tandem by SiO_2-embedded wire molecules, one of them transferring electrons from the LUMO of the light absorber on the oxidizing side to the HOMO of the chromophore on the reducing side (Jo et al. 2022).

3.3 Ultrathin silica membrane with embedded wires for electronic coupling across the biotic/abiotic interface

Ultrathin silica membranes with embedded wires optimized for electron transfer open up the coupling of biotic with abiotic catalysts in nanoscale biohybrids under separation of the two reaction environments. As alluded to in Sect. 2.2, recent progress in the field of bioelectrochemical systems encompasses the synthesis of inorganic chemicals, liquid hydrocarbon fuels and pharmaceuticals using renewable energy sources (Logan and Rabaey 2012; Lu and Ren 2016; Sakimoto et al. 2017; Santoro et al. 2017). Inorganic catalysts and microbial cells can accomplish both oxidation or reduction reactions, and their coupling enables the synthesis of products at high thermodynamic efficiency typically not achieved with either abiotic or biotic approaches alone. In microbial electrolysis cells the organism oxidizes organics, with the generated electrons driving a desired reduction reaction upon transfer to an inorganic catalyst (Rozendal et al. 2009; Lovley 2016). In microbial electrosynthesis cells and biotic/abiotic artificial photosystems, the electrons flow in the opposite direction. Here, the inorganic catalyst performs oxidative catalysis and the microbe conducts reductive chemistry (Nevin et al. 2010; Li et al. 2012; Liu et al. 2016; Sakimoto et al. 2016). A major challenge for any of these bioelectrochemical systems is the incompatibility of the abiotic and biotic catalysis environments. Reactive oxygen species or heavy metal ions emanating from the inorganic

catalyst can damage microbial cells, while the latter can cause corrosion and fouling of the inorganic material or release products like methane or hydrogen that react at the inorganic catalyst (Rosenbaum and Franks 2014; Liu et al. 2016; Sakimoto et al. 2016; Santoro et al. 2017). In currently existing systems, this requires macroscale separation of the abiotic and biotic catalysts or a membrane of µm to mm thickness, resulting in large ohmic losses caused by macroscale ion transport. Ultrathin silica membranes with embedded electron conducting wires provide an opportunity to couple these catalysis environments on the nanometer scale under strict chemical separation thereby drastically reducing these limitations. Moreover, integrating biotic and abiotic catalysts in the form of nano-biohybrids opens up an immense design space for building macroscale systems, which allows to configure bioelectrochemical systems most appropriate for scaleup.

To demonstrate proof-of-principle, we have explored the coupling of the electron-generating *S. oneidensis* MR-1 with inorganic SnO_2 catalyst under separation of the microbial and inorganic environments by an ultrathin silica membrane with embedded wire molecules, as graphically sketched in Figure 14a (Cornejo et al. 2018). This bacterium oxidizes lactate on the inside and transfers the electrons to outer membrane cytochromes with redox potentials in the range -0.2 to 0.2 V vs. NHE (Xu et al. 2016). Extracellular electron transfer to a variety of metal oxides provides energy for cell maintenance and growth. SnO_2 is a semiconductor material with a conduction band around 0 V vs. NHE and therefore a suitable abiotic catalyst component for accepting electrons from *S. oneidensis*. The functionalization of the PV3 wire molecule required strongly electron withdrawing substituents in order to push the LUMO potential from -1.7 V vs. NHE for the unsubstituted oligo(phenylene vinylene) towards less reducing potential. To this end, NO_2 groups were introduced in both outer aryl rings and CN groups substituted in the two

bridging alkene moieties (Figure 14b). CV sweeps of the free wire molecule indicated a LUMO potential positioned around -0.5 V (the actual potential upon covalent attachment of the wire on SnO_2 is likely influenced by electronic interaction with the semiconductor). Similar to the two-step method of PV3 anchoring on other metal oxide surfaces discussed in Sect. 3.1, the wire molecules were attached to the SnO_2 surface by using the silyl aniline tripodal anchor and an amide linkage between PV3 and anchor. The structural integrity and density of the wires (2 nm^{-2}) after casting into 3 nm amorphous SiO_2 by ALD were established by FT-IRRAS, XPS and UV-vis spectroscopic measurements (Cornejo et al. 2018).

Monitoring of the bacterial current from *S. oneidensis* to SiO_2 membrane-embedded wires and SnO_2 nanolayer, deposited by ALD on a Pt electrode, in a microaerobic bioelectrochemical reactor after adding lactate revealed a flow of 0.51 μA cm^{-2}, as shown in Figure 14c (bacterial cell density 0.41 μm cm^{-2}) (Cornejo et al. 2018). This current is 50 times about the average background noise of samples with no wires embedded in the SiO_2 membrane. Another increase of bacterial current when adding more lactate (period 10-24 h in Figure 14c) confirmed that the microbes are the source of electricity. This conclusion was further supported by the absence of current when using PV3 wires with mismatched LUMO (PV3-SO_3, whose LUMO is far too negative), or when using *S. oneidensis ΔmtrB* mutants that lack outer membrane cytochromes and are therefore unable to perform outer membrane electron transfer.

It is important to note that when conducting control CV measurements in the biochemical reactor containing ferro/ferricyanide couple in the aqueous compartment and a Pt/SnO_2/SiO_2 electrode with or without embedded PV3 wires, no $[Fe(CN)_6]^{2+}$ redox wave (0.31 V vs. NHE) was observed. Because the PV3 wire is not accessible to $[Fe(CN)_6]^{2+}$, this observation demonstrates that the 2 nm amorphous SiO_2 membrane completely separates species of the

aqueous solution from the SnO_2 surface. Only the H^+ reduction wave is observed, confirming the proton transport property of amorphous silica layers (Cornejo et al. 2018).

With proof-of-concept of nanoscale separation of an ultrathin separation membrane for bioelectrochemical systems in hand, improvement of the current density is a next goal. The current density is at present about 10 percent of the value for bacterial catalysts on a bare Pt/SnO_2 electrode (inset of Figure 14c). As the optimization of the current density in the case of pure abiotic systems demonstrates (Sect. 2.2), an order of magnitude improvement of electron transfer efficiency can be achieved by optimizing molecular wire density and HOMO energetics. For example, PV3 modification with additional electron withdrawing groups such as CF_3 (Siebbeles and Grozema 2011) for exploring more positive LUMO potentials is of high priority.

4. Conclusions

Ultrathin organic and inorganic separation membranes with embedded molecular wires enable the coupling of photo- and electrocatalytic components on the nanoscale of systems for renewable energy generation or utilization, which represent some of the most important yet challenging chemical transformations. Recent progress in the assembly and the structural characterization by microscopic and spectroscopic methods such as FT-IRRAS is enabling the precise assessment of the composition, structure, and integrity of the membranes under operating conditions. In conjunctions with photoelectrochemical performance evaluation, these tools allow for systematic optimization of molecular wire properties such as energetics, orientation and density for maximum efficiency of charge transport through the membrane.

In the broad area of redox catalysis, ultrathin organic and inorganic membranes with tightly controlled electron transfer properties provide opportunities for developing technologies that overcome longstanding efficiency limitations of existing approaches by coupling incompatible catalytic processes on the shortest possible length scale. The integration of H_2O oxidation and CO_2 reduction reactions in robust inorganic nanoscale units made possible by silica nanomembranes with embedded molecular wires opens up the exploration of artificial photosystems that minimizes efficiency-degrading processes typical for existing approaches (large ohmic losses, blocking of back and side reactions). Similarly, substantial leaps forward are rendered feasible for bioelectrochemical systems that combine the unparalleled efficiency and selectivity of microbial or protein catalysts for synthesizing complex organic molecules with the robustness of inorganic photo- or electrocatalysts: For microbes that convert the chemical energy of waste organics into energetic electrons such as *S. odeinensis*, interfacing with electrodes for generating electricity or coupling to inorganic catalysts for driving synthesis of chemicals on the nanoscale is a promising approach for electrifying industrial processes (microbial electrolysis). Solar light driven synthesis of energy dense hydrocarbon fuels or of major industrial chemicals such as fertilizers using efficient and durable inorganic photocatalysts for delivering electrons by water oxidation coupled to microbial catalysts for CO_2 conversion to multi-carbon products (e.g. *Ralstonia eutropha, Sporomusa ovata*) (Liu et al. 2015; Torella et al. 2015; Liu et al. 2016) is equally promising for overcoming efficiency limitations of existing systems (ohmic losses, prevention of attack of microbes by toxic reactive oxygen species produced at the inorganic catalyst, poisoning of electrocatalysts by leaching metal ions or corrosion by the microbial activity (Logan 2008)) by integration on the nanoscale, enabled by ultrathin electron conducting membranes (microbial photoelectrosynthesis).

Acknowledgments

This work was supported by the Director, Office of Science, Office of Basic Energy Sciences, Division of Chemical, Geological and Biosciences of the US Department of Energy under contract no. DE-AC02-05CH11231. Funding for support of the work on ultrathin silica membranes was in part provided by the Energy and Biosciences Institute through the EBI-Shell program.

References

Baron D, LaBelle E, Coursolle D, Gralnick JA, Bond DR (2009) Electrochemical measurement of electron transfer kinetics by Shewanella oneidensis MR-1. J Biol Chem 284:28865-28873. https://doi.org/10.1074/jbc.M109.043455

Burton BB, Kang SW, Rhee SW, George SM (2009) SiO_2 atomic layer deposition using tris(dimethylamino)silane and hydrogen peroxide studied by in situ transmission FT-IR spectroscopy. J Phys Chem C 113:8249-8257. https://doi.org/10.1021/jp806638e

Chabal YJ (1988) Surface infrared spectroscopy. Surf Sci Rep 8:211-357. https://doi.org/10.1016/0167-5729(88)90011-8

Cornejo JA, Sheng H, Edri E, Ajo-Franklin CM, Frei H (2018) Nanoscale membranes that chemically isolate and electronically wire up the abiotic/biotic interface. Nat Commun 9:2263. http://doi.org/10.1038/s41467-018-04707-6

Coursolle D, Baron DB, Bond DR, Gralnick JA (2010) The Mtr respiratory pathway is essential for reducing flavins and electrodes in Shewanella oneidensis. J Bacteriol 192:467-474. https://doi.org/10.1128/JB.00925-09

Du J, Thomas AW, Chen X, Garner LE, Vandenberg CA, Bazan GC (2013) Increased ion conductance across mammalian membranes modified with conjugated oligoelectrolytes. Chem Commun 49:9624-9626. https://doi.org/10.1039/c3cc45094e

Edri E, Aloni S, Frei H (2018) Fabrication of core-shell nanotube array for artificial photosynthesis featuring an ultrathin composite separation membrane. ACS Nano 12:533-541. https://doi.org/10.1021/acsnano.7b07125

Edri E, Cooper JK, Sharp ID, Guldi DM, Frei H (2017) Ultrafast charge transfer between light absorber and Co_3O_4 water oxidation catalyst across molecular wires embedded in silica membrane. J Am Chem Soc 139:5458-5466. https://doi.org/10.1021/jacs.7b01070

El-Naggar MY, Wanger G, Leung KM, Yuzvinsky TD, Southam G, Yang J, Lau WM, Nealson KH, Gorby YA (2010) Electrical transport along bacterial nanowires from Schewanella oneidensis MR-1. Proc Natl Acad Sci USA 107:18127-18131. https://doi.org/10.1073/pnas.1004880107

Frei H (2023) Ultrathin electron and proton-conducting membranes for nanoscale integrated artificial photosystems. Sustain Energy Fuels 7:3213-3231. https://doi.org/10.1039/d3se00499f

Garner LE, Park J, Dyar, SM, Chworos A, Summer JJ, Bazan GC (2010) Modification of the optoelectronic properties of membranes via insertion of amphiphilic phenylenevinylene oligoelectrolytes. J Am Chem Soc 132:10042-10052. https://doi.org/10.1021/ja1016156

Gaylord BS, Wang S, Heeger, AJ, Bazan GC (2001) Water-soluble conjugated oligomers: Effect of chain length and aggregation on photoluminescence-quenching efficiencies. J Am Chem Soc 123:6417-6418. https://doi.org/10.1021/ja010373f

Hollins P (2006) Infrared reflection absorption spectroscopy. In: Meyers RA (ed) Encyclopedia of Analytical Chemistry, Wiley, New York, pp 1-19.

Hou H, Chen X, Thomas AW, Catania C, Kirchhofer ND, Garner LE, Han A, Bazan GC (2013) Conjugated oligoelectrolytes increase power generation in E. coli microbial fuel cells. Adv Mater 25:1593-1597. https://doi.org/10.1002/adma.201204271

Jo WJ, Katsoukis G, Frei H (2020) Ultrathin amorphous silica membrane enhances proton transfer across solid-to-solid interfaces of stacked metal oxide nanolayers while blocking oxygen. Adv Funct Mater 30:190262. https://doi.org/10.1002/adfm.201909262

Jo WJ, Zhang H, Katsoukis G, Frei H (2022) Ultrathin silica layers as separation membranes for artificial photosynthesis. In: Frei H, Esposito DV (eds) Ultrathin oxide layers for solar and electrocatalytic systems, Energy Environ Ser, Vol 30, The Royal Society of Chemistry, London, pp. 298-341. https://doi.org/10.1039/9781839163708

Katsoukis G, Frei H (2018) Heterobinuclear light absorber coupled to molecular wire for charge transport across ultrathin silica membrane for artificial photosynthesis. ACS Appl Mater Interfaces 10:31422-31432. https://doi.org/10.1021.acsami.8b11684

Katsoukis G, Jo WJ, Frei H (2019) Structure and orientation of molecular wires embedded in ultrathin silica membrane for artificial photosynthesis elucidated by polarized FT-IRRAS. J Phys Chem C 123:18905-18913. https://doi.org/10.1021/acs.jpcc.9b02523

Kim W, Edri E, Frei H (2016) Hierarchical inorganic assemblies for artificial photosynthesis. Acc Chem Res 49:1634-1645. https://doi.org/10.1021/acs.accounts.6b00182

Kim W, McClure BA, Edri E, Frei H (2016) Coupling of carbon dioxide reduction with water oxidation in nanoscale photocatalytic assemblies. Chem Soc Rev 45:3221-3243. https://doi.org/10.1039/c6cs00062b

Kirchhofer ND, Chen X, Marsili E, Sumner JJ, Dahlquist FW, Bazan GC (2014) The conjugate oligoelectrolyte DSSN+ enables exceptional coulombic efficiency via direct electron transfer for anode-respiring Shewanella oneidensis MR-1, a mechanistic study. Phys Chem Chem Phys 16:20436-20443. https://doi.org/10.1039/c4cp03197k

Krassen H, Schwarze A, Friedrich B, Ataka K, Lenz O, Heberle J (2009) Photosynthetic hydrogen production by a hybrid complex of photosystem I and [NiFe]-hydrogenase. ACS Nano 3:4055-4061. https://doi.org/10.1021/nn900748j

Lee Y, Yang I, Lee JE, Hwang S, Lee JW, Um SS, Nguyen TL, Yoo PJ, Woo, HY, Park J, Kim SK (2013) Enhanced photocurrent generation by Foerster resonance energy transfer between phospholipid-assembled conjugated oligoelectrolytes and nile red. J Phys Chem C 117:3298-3307. https://doi.org/10.1021/jp3117193

Li H, Opgenorth PH, Wernick DG, Rogers S, Wu TY, Higashide W, Malati P, Huo YX, Cho KM, Liao JC (2012) Integrated electromicrobial conversion of CO_2 to higher alcohols. Science 335:1596. https://doi.org/10.1126/science.1217643

Liu C, Colon BC, Ziesack M, Silver PA, Nocera DG (2016) Water splitting-biosynthetic system with CO_2 reduction efficiencies exceeding photosynthesis. Science 352:1210-1213. https://doi.org/10.1126/science.aaf5039

Liu C, Gallagher JJ, Sakimoto KK, Nichols EM, Chang CJ, Chang MCY, Yang P (2015) Nano Lett 15:3634-3639. https://doi.org/10.1021/acs.nanolett.5b01254

Logan BE (2008) Microbial Fuel Cells, 1st edn. Wiley, Hoboken, pp. 85-110.

Logan BE and Rabaey K (2012) Conversion of wastes into bioelectricity and chemicals by using microbial electrochemical technologies. Science 337:686-690. https://doi.org/10.1126/science.121741 2

Lovley DR (2016) Happy together: microbial communities that hook up to swap electrons. ISME 11:327-336. https://doi.org/10.1038/ismej.2016.136

Lovley DR (2008) The microbe electric: conversion of organic matter to electricity. Curr Opin Biotech 19:564-571. https://doi.org/10.1016/j.copbio.2008.10.005

Lu L and Ren ZJ (2016) Microbial electrolysis cells for waste biorefinery: a state of the art review. Bioresour Technol 215:254-264. https://doi.org/10.1016/j.biortech.2016.03.034

Manocchi AK, Baker DR, Pendley SS, Nguyen K, Hurley MM, Bruce BD, Sumner JJ, Lundgren CA (2013) Photocurrent generation from surface assembled photosystem I on alkanethiol modified electrodes. Langmuir 29:2412-2419. https://doi.org/10.1021/la304477u

Marcus RA and Sutin N (1985) Electron transfers in chemistry and biology. Biochim Biophys Acta 811:265-322. https://doi.org/10.1016/0304-4173(85)90014-X

Marsili E, Baron DB, Shikhare ID, Coursolle D, Gralnick JA, Bond D (2008) Shewanella secretes flavins that mediate extracellular electron transfer. Proc Natl Acad Sci USA 105:3968-3973. https://doi.org/10.1073/pnas.0710525105

Nevin KP, Woodard TL, Franks AE, Summers ZM, Lovley DR (2010) Miccrobial electrosynthesis: Feeding microbes electricity to convert carbon dioxide and water to multicarbon extracellular organic compounds. mBio 1:e00103-e00110. https://doi.org/10.1128/mBio.00103-10

Okamoto A, Hashimoto K, Nealson KH, Nakamura R (2013) Rate enhancement of bacterial extracellular electron transport involved bound flavin semiquinones. Proc Natl Acad Sci USA 110:7856-7861. https://doi.org/10.1073/pnas.1220823110

Rabaey K and Rozendal RA (2010) Microbial electrosynthesis - revisiting the electrical route for microbial production. Nat Rev Microbiol 8:706-716. https://doi.org/10.1038/nrmicro2422

Rosenbaum MA and Franks AE (2014) Microbial catalysis in bioelectrochemical technologies: status quo, challenges and perspectives. Appl Microbiol Biotechnol 98:509-518. https://doi.org/10.1007/s00253-013-5396-6

Roy JN, Babanova S, Garcia KE, Cornejo J, Ista LK, Atanassov P (2014) Catalytic biofilm formation by Schewanella oneidensis MR-1 and anode characterization by expanded uncertainty. Electrochim Acta 126:3-10. https://doi.org/10.1016/j.electacta.2013.07.075

Rozendal RA, Leone E, Keller J, Rabaey K (2009) Efficient hydrogen peroxide generation from organic matter in a bioelectrochemical system. Electrochem Commun 11:1752-1755. https://doi.org/10.1016/j.elecom.2009.07.008

Saboe PO, Conte E, Chan S, Feroz H, Ferlez B, Farell M, Poyton MF, Sines IT, Yan H, Bazan GC, Golbeck J, Kumar M (2016) Biomimetic wiring and stabilization of photosynthetic membrane proteins with block copolymer interfaces. J Mater Chem A 4:15457-15463. https://doi.org/10.1039/c6ta07148a

Saboe PO, Lubner CE, McCool NS, Vargas-Barbosa NM, Yan H, Chan S, Ferlez B, Bazan GC, Golbeck JH, Kumar M (2014) Two-dimensional protein crystals for solar energy conversion. Adv Mater 26:7064-7069. https://doi.org/10.1002/adma.201402375

Sakimoto KK, Kornienko N, Yang P (2017) Cyborgian material design for solar fuel production: The emerging photosynthetic biohybrid systems. Acc Chem Res 50:476-481. https://doi.org/10.1021/acs.accounts.6b00483

Sakimoto KK, Wong AB, Yang P (2016) Self-photosensitization of non-photosynthetic bacteria for solar-to-chemical production. Science 351:74-77. https://doi.org/10.1126/science.aad3317

Santoro C, Arbizzani C, Erable B, Ieropoulos I (2017) Microbial fuel cells: from fundamentals to applications. A review. J Power Sources 356:225-244. https://doi.org/10.1016/j.jpowsour.2017.03.109

Siebbeles LDA and Grozema FC (eds) (2011) Charge and exciton transport through molecular wires. Wiley, New York

Son HJ, Wang X, Prasittichai C, Jeong NC, Aaltonen T, Gordon RG, Hupp JT (2012) Glass-encapsulated light harvesters: more efficient dye-sensitized solar cells by deposition of self-

aligned, conformal, and self-limited layers. J Am Chem Soc 134:9537-9540. https://doi.org/10.1021/ja300015n

Sun K, Moreno-Hernandez IA, Schmidt WC, Zhou X, Crompton JC, Liu R, Saadi FH, Chen Y, Papadantonakis KM, Lewis NS (2017) A comparison of the chemical, optical and electrocatalytic properties of water oxidation catalysts for use in integrated solar fuel generators. Energy Environ Sci 10:87-1002. https://doi.org/10.1039/c6ee03563a

Thomas AW, Garner LE, Nevin KP, Woodard TL, Franks AE, Lovley DR, Sumner JJ, Sund CJ, Bazan GC (2013) A lipid membrane intercalating conjugated oligoelectrolytes enables electrode driven succinate production in Shewanella. Energy Environ Sci 6:1761-1765. https://doi.org/10.1039/c3ee00071k

Torella JP, Gagliardi CJ, Chen JS, Bediako DK, Colon B, Way JC, Silver PA, Nocera DG (2015) Proc Natl Acad Sci USA 112:2337-2342. https://doi.org/10.1073/pnas.1424872112

Woo HY, Liu B, Kohler B, Korystov D, Mikhailovsky A, Bazan GC (2005) Solvent effects on the two-photon absorption of distyrylbenzene chromophores. J Am Chem Soc 127:14721-14729. https://doi.org/10.1021/ja052906g

Xu S, Jangir Y, El-Naggar MY (2016) Disentangling the roles of free and cyctochrome-bound flavins in extracellular electron transport from Shewanella oneidensis MR-1. Electrochim Acta 198:49-55. https://doi.org/10.1016/j.electacta.2016.03.074

Yan H, Catania C, Bazan GC (2015) Membrane-intercalating conjugated oligoelectrolytes: Impact on bioelectrochemical systems. Adv Mater 27:2958-2973. https://doi.org/10.1002/adma.201500487

Zhang H, Weiss I, Rudra I, Jo WJ, Kellner S, Katsoukis G, Galoppini E, Frei H (2021) Controlling and optimizing photoinduced charge transfer across ultrathin silica separation

membrane with embedded molecular wires for artificial photosynthesis. ACS Appl Mater Interfaces 13:23532-23546. https://doi.org/10.1021/acsami.1c00735

Zhou C, Chia GWN, Yong KT (2022) Membrane-intercalating conjugated oligoelectrolytes. Chem Soc Rev 51:9917-9932. https://doi.org/10.1039/d2cs00014h

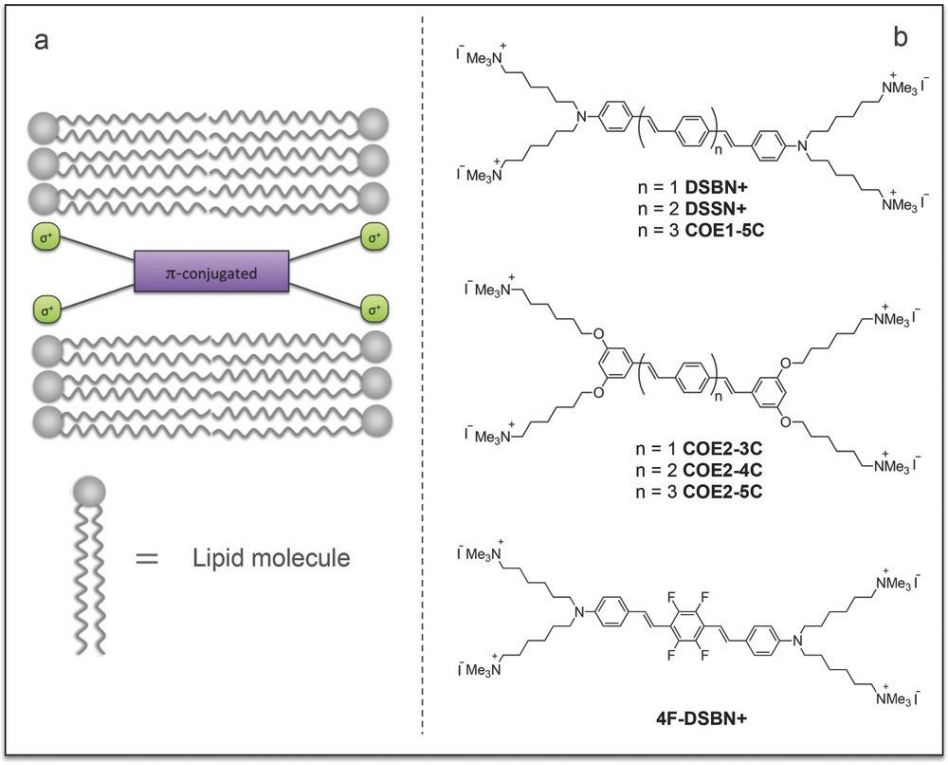

Figure 1 Conjugated oligoelectrolytes in lipid bilayer membranes. a) Schematic of oligo(phenylenevinylene) wire molecule intercalated in DPPC lipid bilayer. b) Oligo(phenylenevinylene) structures of various lengths and functionalization. Reproduced from Yan et al. 2015 with permission from WILEY-VCH Verlag GmbH & Co. KGaA, Weinheim

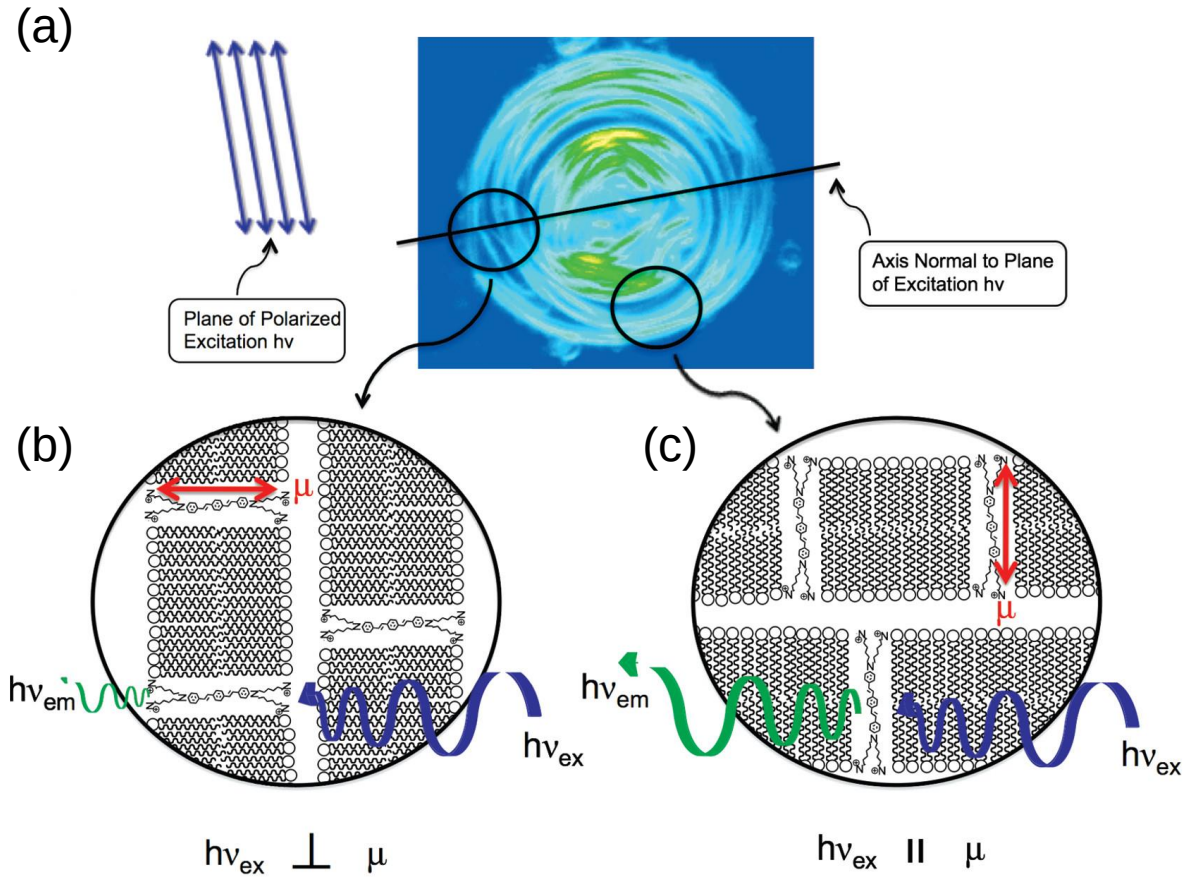

Figure 2 Structural characterization of molecular wires embedded in lipid bilayers. (a) Confocal fluorescence microscopic image of a stationary multilamellar DMPC vesicle (diameter = ~15 μm) containing DSBN+ wires that exhibits an equatorial extinction line (black line) perpendicular to the plane of the 488 nm Ar laser excitation light. (b) Close-up view within the extinction line region in which DSBN+ molecules are oriented with their transition dipoles perpendicular to the plane of the excitation light resulting in attenuated emission. (c) Close-up view within the regions above and below the extinction line in which DSBN+ transition dipoles are oriented parallel to the plane polarized excitation light resulting in a greater number of excited states and stronger emission. Reproduced from Yan et al. 2015 with permission from WILEY-VCH Verlag GmbH & Co. KGaA, Weinheim

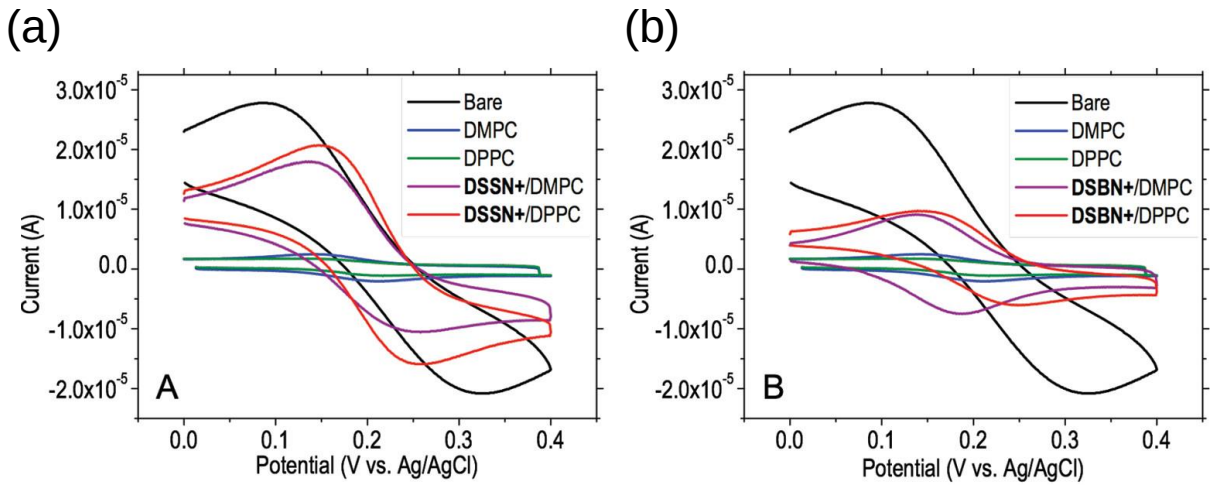

Figure 3 Evaluation of electron transfer of bilayer embedded wire molecules by CV. (a) CV sweeps of DMPC and DPPC bilayers with embedded DSSN+ wires exposed to ferricyanide/ferrocyanide aqueous electrolyte and of control samples without DSSN+. The CV wave for ferricyanide solution exposed to a bare glassy carbon electrode is also shown. (b) Analogous CV measurements for bilayers featuring the shorter DSBN+ embedded wire. Reproduced from Garner et al. 2010 with permission from the American Chemical Society

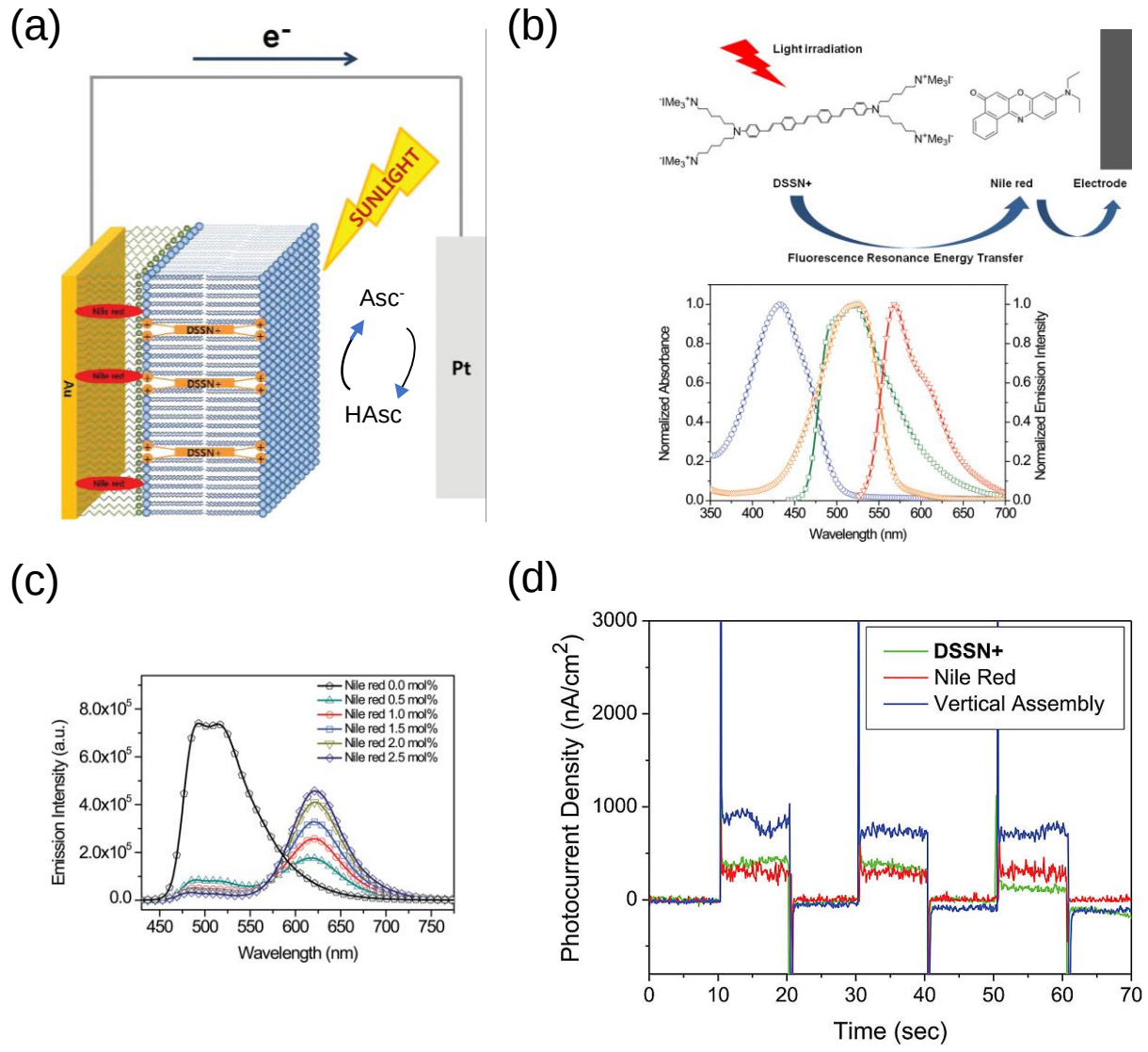

Figure 4 Photovoltaic efficiency enhancement by Foerster resonance energy transfer (FRET) of intercalated visible dye. (a) Photoelectrochemical system featuring Au anode covered by alkane thiol film with embedded Nile red dye, which is interfaced with DMPC/DSSN+ lipid bilayer. (b) FRET process, overlap of optical absorption of Nile red with DSSN+ wire emission. (c) Linear increase of Nile red emission with increasing dye concentration (DSSN+ excitation at 400 nm). (d) Anodic photocurrent of photoelectrochemical system shown in (a) (blue trace), only DMPC/DSSN+ lipid bilayer (green trace), and only alkane thiol/Nile red film (red trace). Reproduced from Lee et al. 2013 with permission from the American Chemical Society

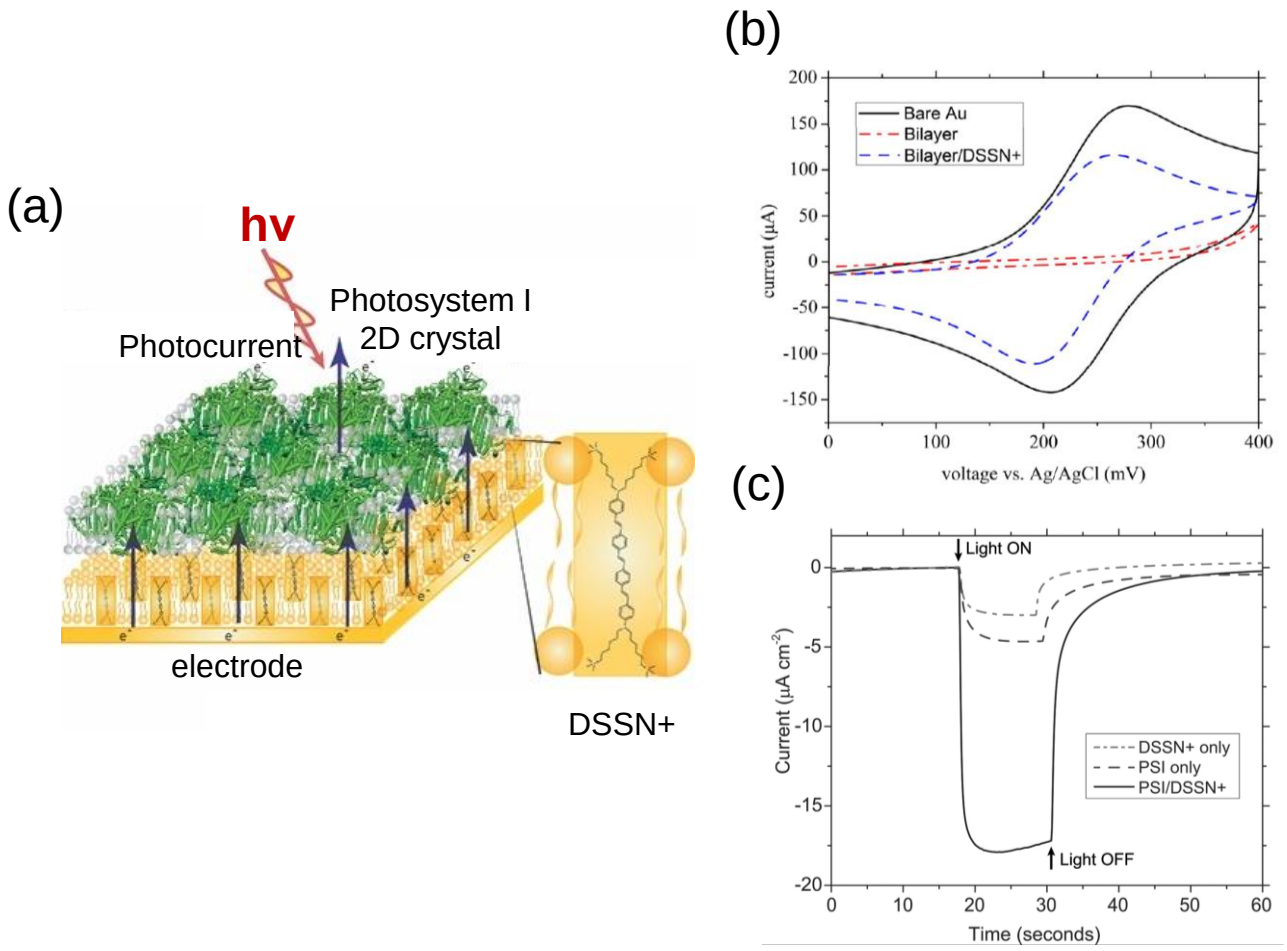

Figure 5 PSI protein complex interfaced with a lipid bilayer/DSSN+ membrane on a Au electrode. (a) Schematic of assembly of PSI 2D array on electron conducting bilayer membrane deposited on electrode surface. (b) CV sweep of PSI-bilayer/DSSN+ electrode exposed to ferricyanide/ferrocyanide solution (dashed blue trace). No CV wave is observed for electrodes lacking intercalated DSSN+ (dashed red trace). CV of ferricyanide/ferrocyanide solution exposed to bare Au electrode is also shown (black trace). (c) Photocurrent of PSI-bilayer/DSSN+ cathode for MV^{2+} reduction (solid trace, -0.3 V vs. Ag/AgCl). Control runs in the absence of DSSN+ (dashed trace) or in the absence of PSI (dashed-dot trace) are also shown. Reproduced from Saboe et al. 2014 with permission from WILEY-VCH Verlag GmbH & Co. KGaA, Weinheim

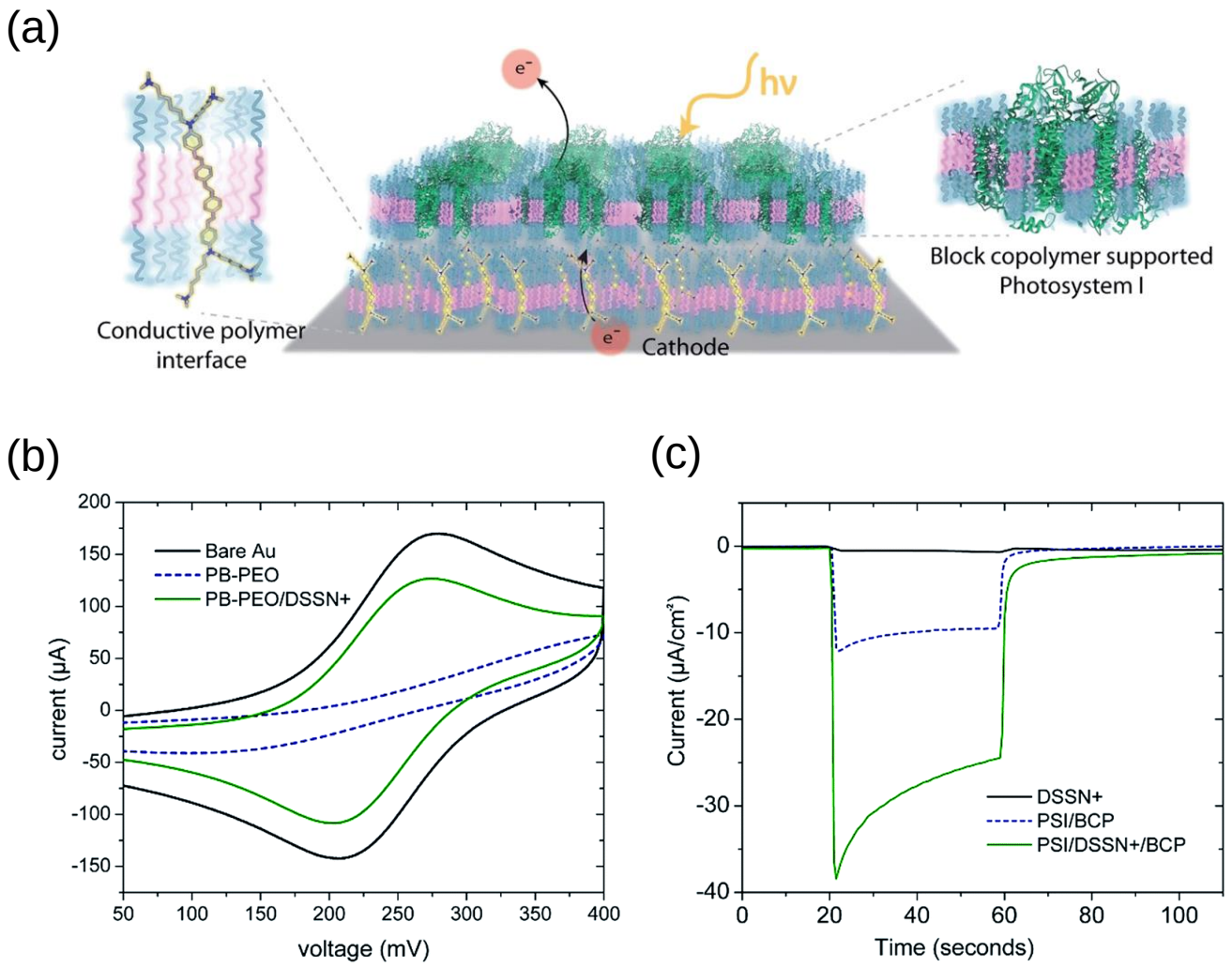

Figure 6 PSI protein complex interfaced with a block copolymer bilayer/DSSN+ membrane on a Au electrode. (a) Schematic of assembly of PSI incorporated at high density in a block copolymer layer and interfaced with electron conducting bilayer membrane deposited on the Au cathode surface. (b) CV sweep of PSI-block copolymer bilayer/DSSN+ electrode exposed to ferricyanide/ferrocyanide solution (green solid trace). No CV wave is observed for electrodes lacking a block copolymer/DSSN+ membrane (blue dotted trace). CV of ferricyanide/ferrocyanide solution exposed to bare Au electrode is also shown (black trace). (c) Photocurrent of PSI-block copolymer bilayer/DSSN+ cathode on Au electrode (green solid trace). Control photocurrent runs shown are for electrode lacking block copolymer/DSSN+ layer (blue dotted trace) or lacking PSI (black solid trace). Reproduced from Saboe et al. 2016 with permission from the Royal Society of Chemistry

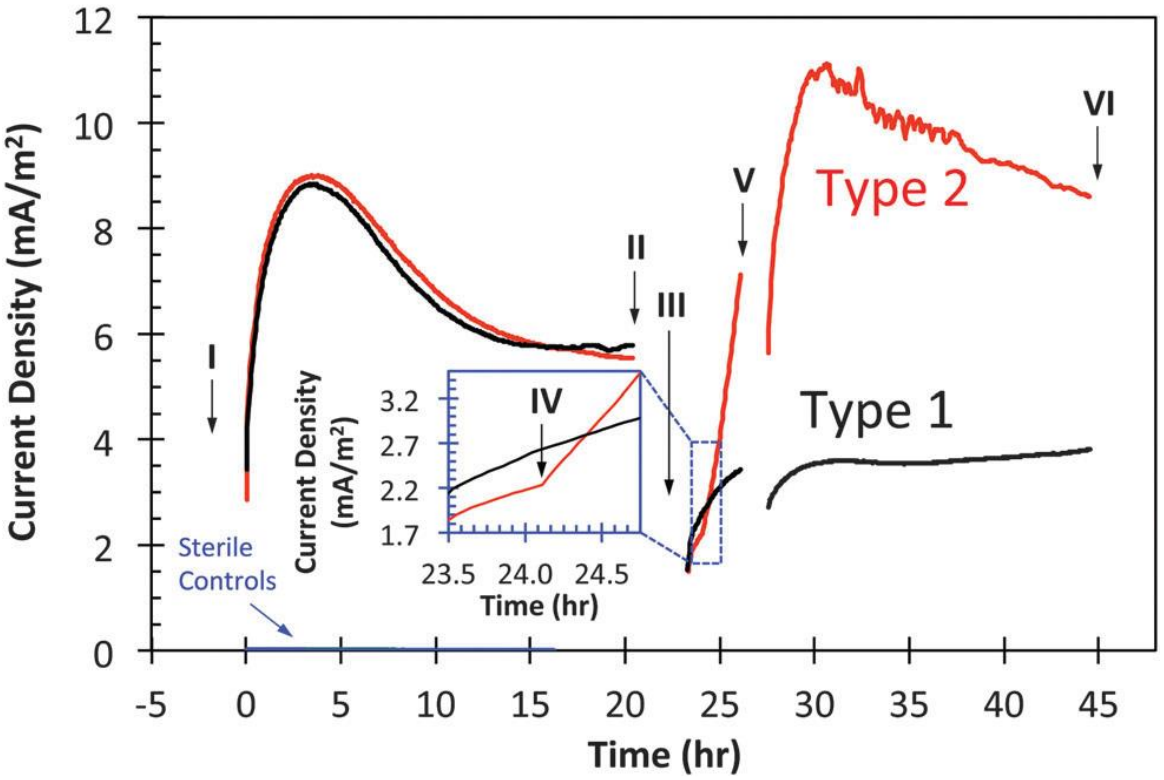

Figure 7 Bacterial current of *Shewanella oneidensis* interacting with lipid bilayer/DSSN+ membrane deposited on graphite anode. Left hand curves: Current density behavior of 2 identical samples (red and black traces) held at +0.2 V vs. Ag/AgCl upon addition of lactate at time point marked I, with stop at point II. Right hand curves: Current density behavior of a fresh sample with 5 µM DSSN+ added when exposing to lactate (red trace, start at IV, stop at VI) compared with current behavior for an identical sample but without DSSN+ (black trace). Inset: Instant current boosting effect for the sample with DSSN+ wires is shown (time point IV). Reproduced from Kirchhofer et al. 2014 with permission from the Royal Society of Chemistry

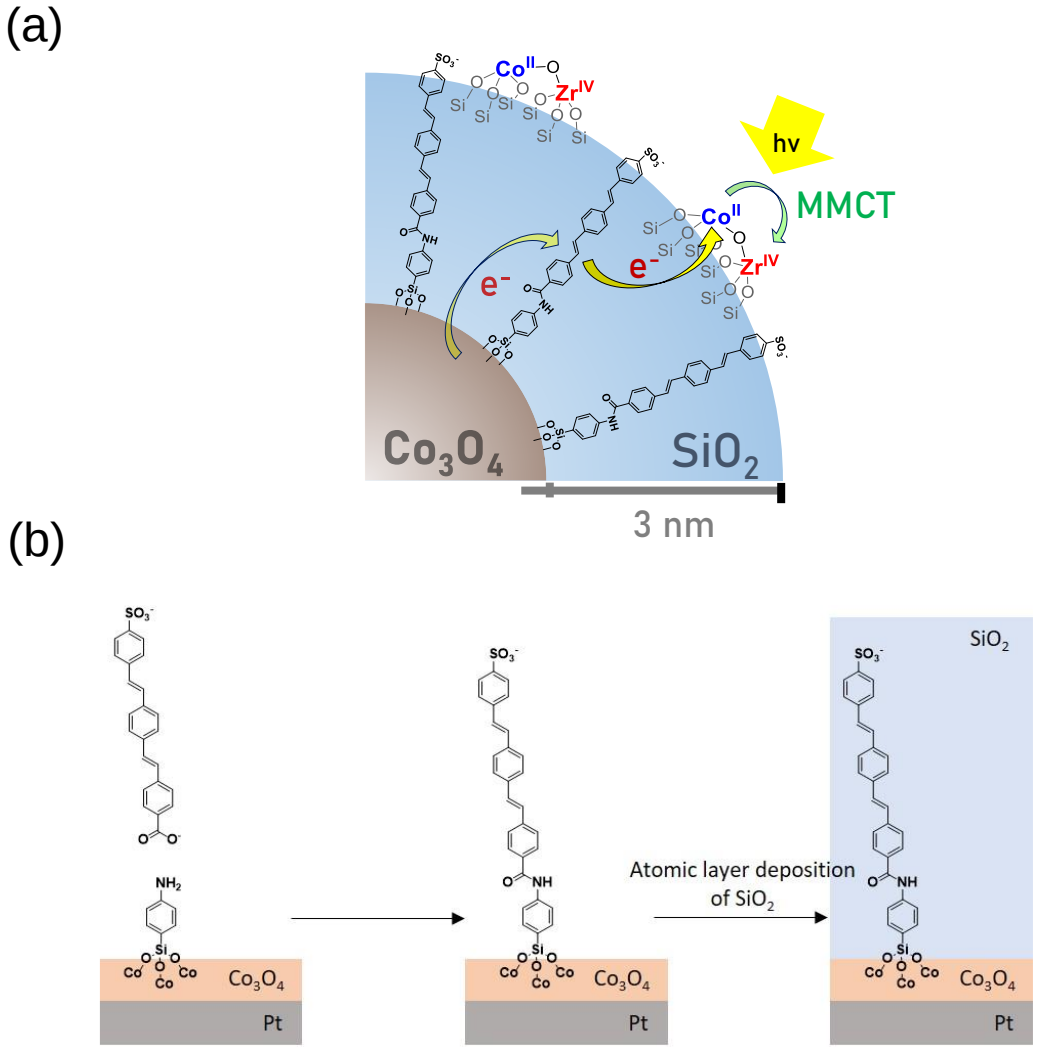

Figure 8 Ultrathin amorphous silica membrane with embedded molecular wires for separating Co oxide H_2O oxidation catalyst from light absorber and sites of CO_2 reduction catalysis. (a) Schematic of visible light driven hole transfer from transient Co^{III} formed by $Zr^{IV}OCo^{II} \rightarrow Zr^{III}OCo^{III}$ metal-to-metal charge-transfer excitation via embedded PV3 wire to the Co_3O_4 catalyst. Transient Zr^{III} reduces CO_2 to CO. (b) Method of wire attachment to Co_3O_4 surface using TMSA anchor and amide linkage for PV3 attachment, followed by ALD of amorphous SiO_2. Reproduced from Katsoukis and Frei 2018, and Katsoukis et al. 2019 with permission from the American Chemical Society

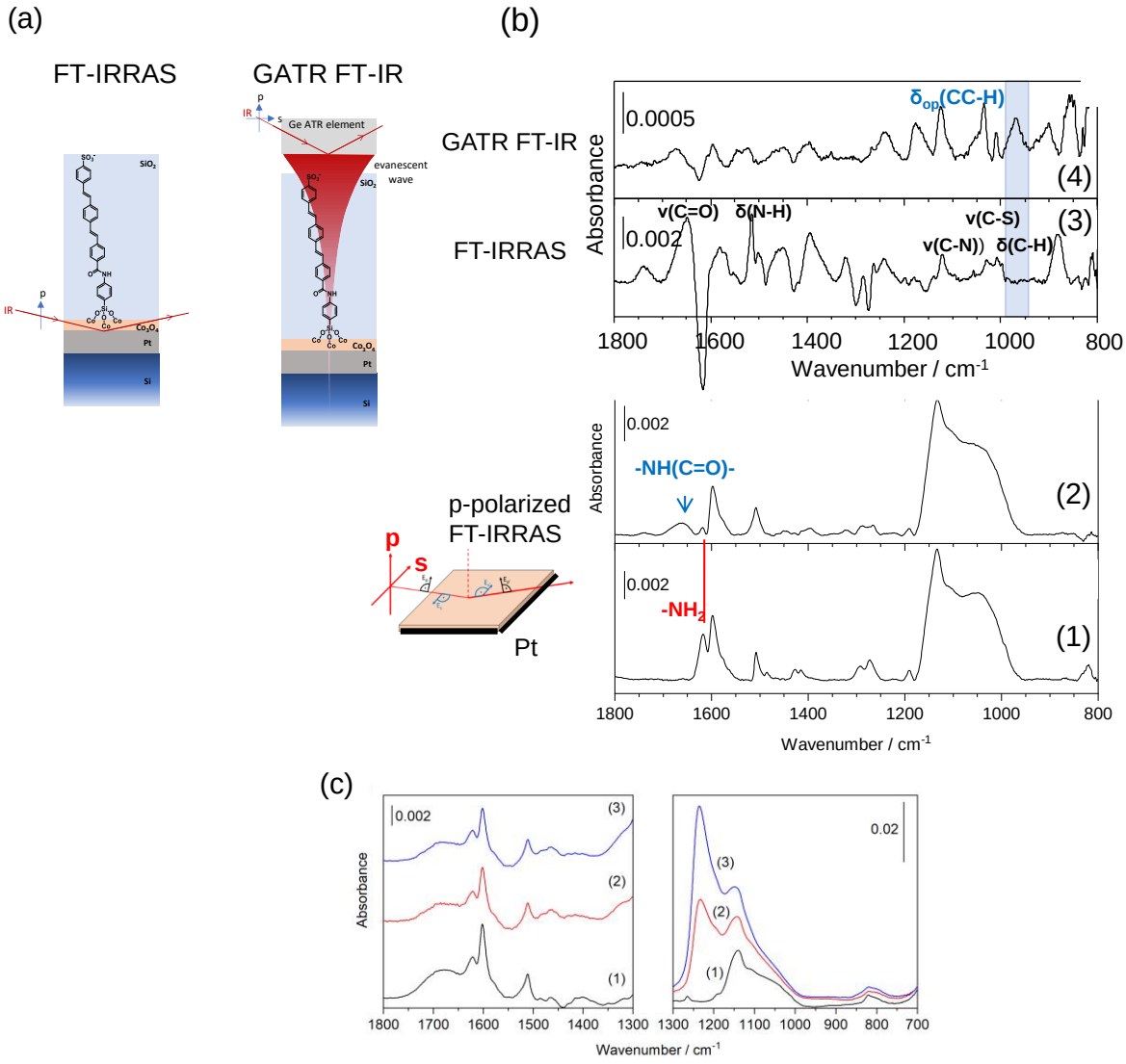

Figure 9 Infrared monitoring of PV3 wire attachment to Co_3O_4 surface and casting into silica. (a) Schematic showing the principle of FT-IRRAS and GATR FT-IR spectroscopy. (b) FT-IRRAS of TMSA anchored on Co_3O_4 (1) and after attachment of PV3 (2). Trace (3) shows the same sample as (2) but with TMSA bands subtracted. Trace (4) is the GATR FT-IR spectrum of the same sample shown in trace (3). (c) FT-IRRAS of PV3 anchored on Co_3O_4 before (black trace (1)) and after ALD of 3 nm of SiO_2 (red trace (2)). The blue trace (3) shows the spectrum after ALD of additional 3 nm SiO_2. Reproduced from Katsoukis et al. 2019 with permission from the American Chemical Society

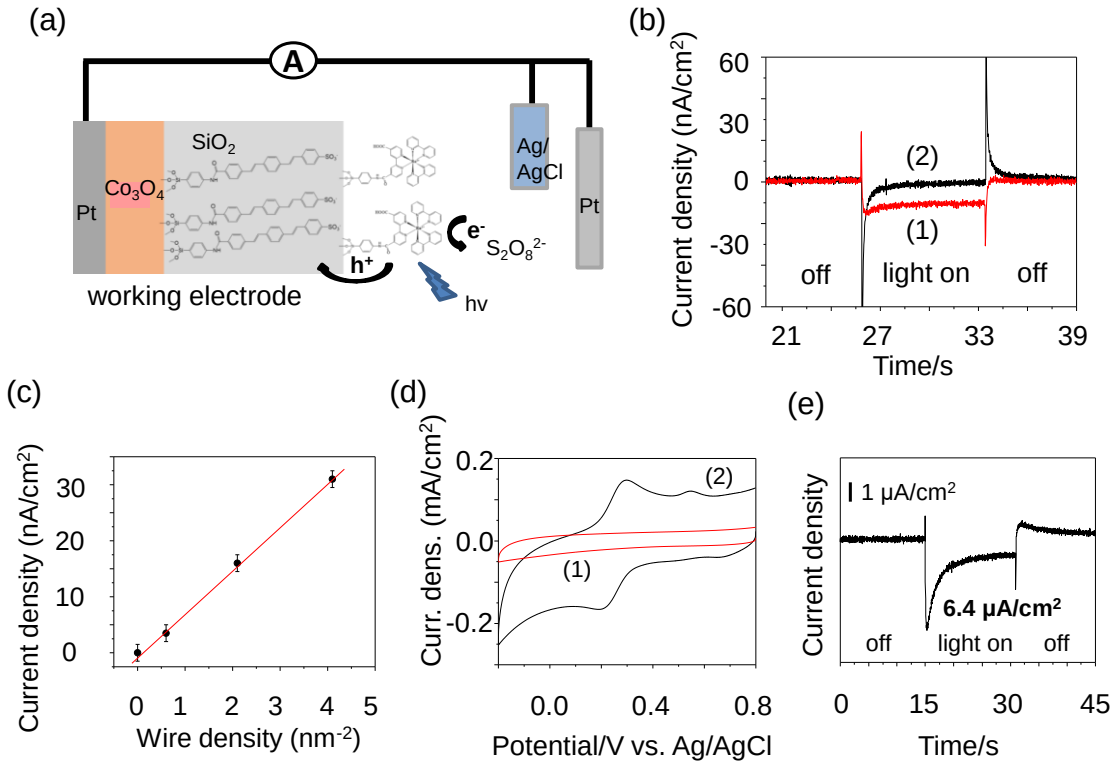

Figure 10 Short-circuit photocurrent measurements for determining electron conductivity. (a) Schematic of a 3-electrode cell with a working Pt electrode onto which 12 nm Co_3O_4 followed by a 3 nm silica membrane with embedded wire were deposited. Anchored $[Ru(bpy_2)(dcbpy)]^{2+}$ light absorbers are also shown. (b) Current density measurement upon visible light excitation of the photocathode assembly shown in (a) (red trace (1)) and the assembly without embedded PV3 wires (black trace (2)). (c) Wire density dependence of the photocurrent. (d) CV of $Pt/Co_3O_4/PV3/SiO_2$ working electrode exposed to $Fe(CN)_6^{3-}$ solution (red trace (1)) and after deliberately introducing pinholes (black trace (2)). (e) Photocurrent for visible light irradiation of sample shown in (a) after replacing persulfate acceptor by TiO_2 nanolayer (5 nm) deposited on SiO_2 membrane. Reproduced from Zhang et al. 2021 with permission from the American Chemical Society

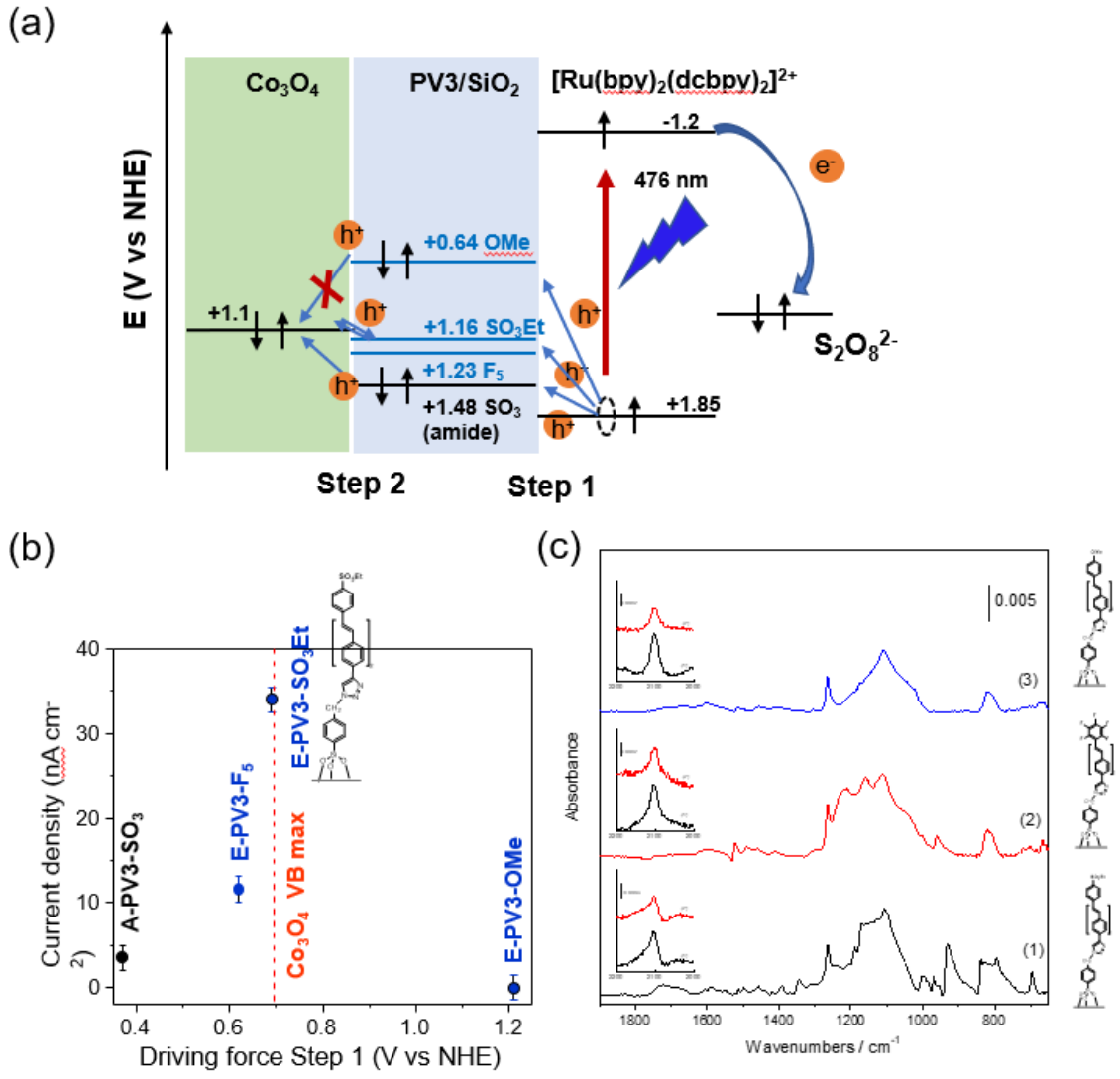

Figure 11 Optimization of energy level alignment of molecular wires. (a) HOMO potentials of modified wires and their position relative to light absorber and catalyst potentials. Wire labeling described in text. (b) Photocurrent dependence on HOMO potential of embedded wire molecule, normalized for wire density of 0.6 nm^{-2}. (c) FT-IRRAS of triazole-linked wires anchored on Co_3O_4 catalyst surface. The insets show the decrease of the azide stretch mode at 2100 cm^{-1}: black trace, before PV3 attachment; red trace, after triazole linkage formation. Reproduced from Zhang et al. 2021 with permission from the American Chemical Society

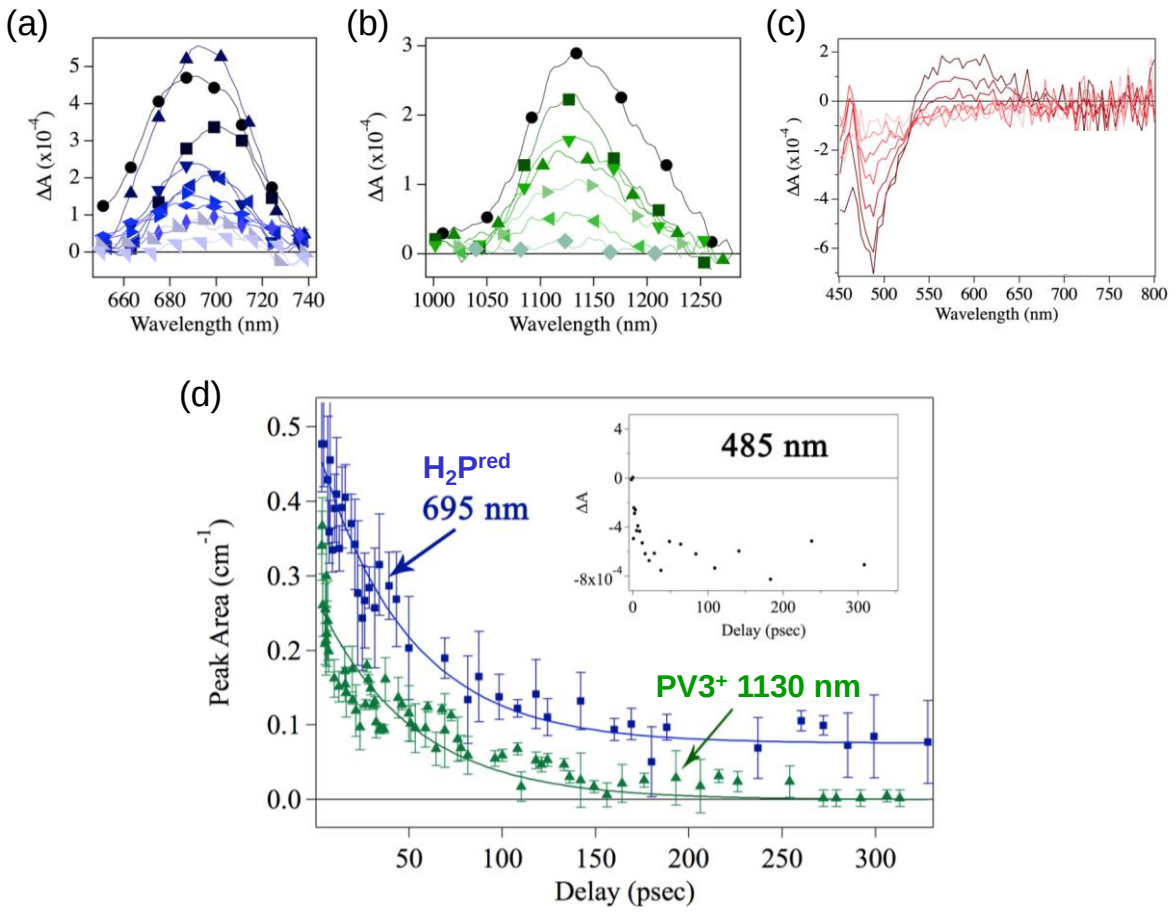

Figure 12 Ultrafast optical absorption spectroscopy of visible light-induced hole transfer across silica membrane via embedded wire molecules. Transient absorption and decay of (a) reduced porphyrin (H_2P^{red}, 695 nm); (b) hole charge on wire ($PV3^+$, 1130 nm); (c) hole charge on Co_3O_4 (bleach at 485 nm; the spectral traces show the decay on the hundreds of ns time scale). (d) Detailed kinetics of $PV3^+$ and H_2P^{red} decay. The inset shows the growth kinetics of the 485 nm bleach upon hole transfer from $PV3^+$ to Co_3O_4. Reproduced from Edri et al. 2017 with permission from the American Chemical Society

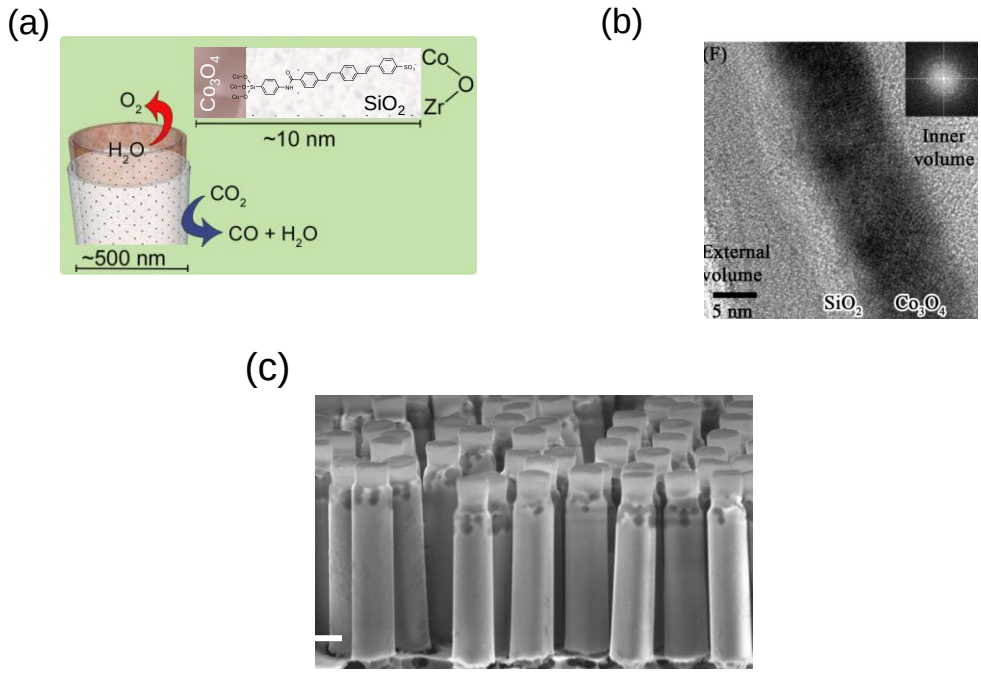

Figure 13 Co oxide-silica core-shell nanotube as complete photosynthetic unit with built-in membrane separation for CO_2 photoreduction by H_2O. (a) Schematic of the design. (b) HR-TEM image showing longitudinal cross-section of single Co_3O_4-SiO_2 core-shell nanotube wall. Inset: fast Fourier transform image of the crystalline Co_3O_4 layer. (c) SEM of a section of the square inch-sized $Co_3O_4/SiO_2/TiO_2$ nanotube array. Scale bar: 500 µ. Reproduced from Edri et al. 2018 with permission from the American Chemical Society

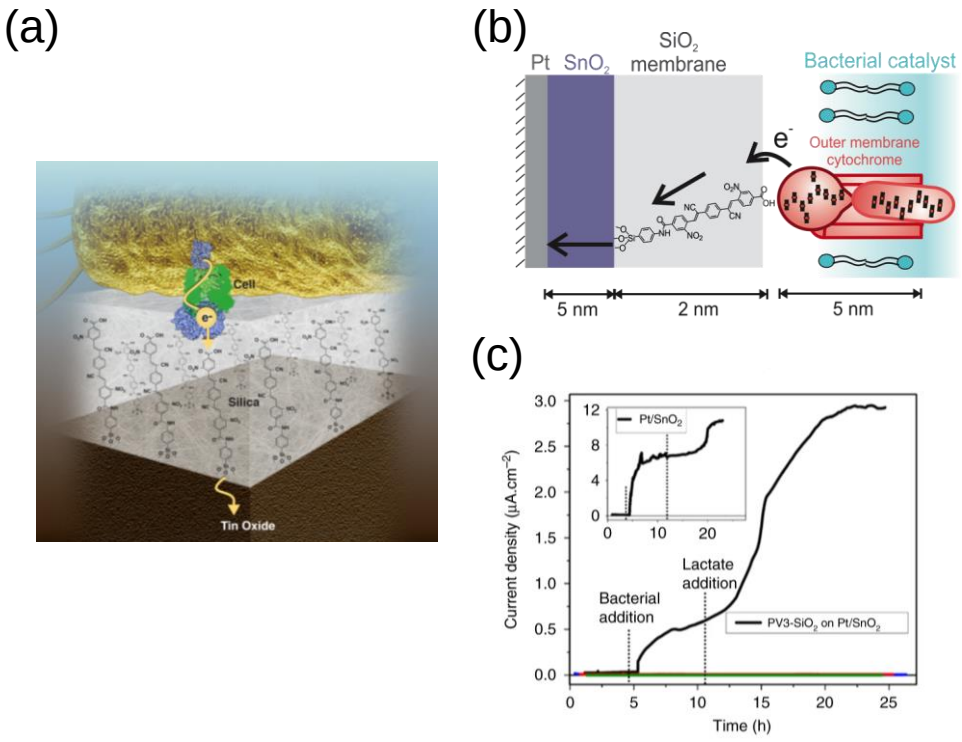

Figure 14 Ultrathin silica membrane with embedded molecular wires for electronic coupling across the biotic/abiotic interface. (a) Schematic of *S. oneidensis* coupled to SnO_2 catalyst via silica-embedded PV3 wires. (b) Electrons are transferred from microbial outer membrane cyctochrome c to the LUMO of the molecular wire and then to the inorganic catalyst. (c) Chronoamperometry at +0.6 V vs. of *S. oneidensis* on SiO_2-encapsulated PV3 on Pt/SnO_2 electrode (black trace). Control experiments: pure SiO_2 (no wires) on Pt/SnO_2 electrode (blue trace); SiO_2-encapsulated unmodified PV3 wires with too negative LUMO potential (red trace); *S. oneidensis ΔmtrB* mutant with SiO_2-encapsulated proper PV3 wires on Pt/SnO_2 electrode (green trace). Onset of current coincides with addition of *S. oneidensis* to the electrochemical cell after a period of current stabilization. Second rise of current indicates addition of lactate. Inset: *S. oneidensis* on Pt/SnO_2 (bare anode). Reproduced from Cornejo et al. 2018 with permission from Springer Nature